Effect of the third invariant on the formation of necking instabilities in ductile plates subjected to plane strain tension

J. A. Rodríguez-Martínez[a,*], O. Cazacu[b], N. Chandola[b], K. E. N'souglo[a]

[a] *Department of Continuum Mechanics and Structural Analysis. University Carlos III of Madrid. Avda. de la Universidad, 30. 28911 Leganés, Madrid, Spain*

[b] *Department of Mechanical and Aerospace Engineering, University of Florida, REEF, 1350 N. Poquito Rd., Shalimar, FL 32579, USA*

Abstract

In this paper, we have investigated the effect of the third invariant of the stress deviator on the formation of necking instabilities in isotropic metallic plates subjected to plane strain tension. For that purpose, we have performed finite element calculations and linear stability analysis for initial equivalent strain rates ranging from 10^{-4} s^{-1} to $8 \cdot 10^4$ s^{-1}. The plastic behavior of the material has been described with the isotropic Drucker yield criterion [11], which depends on both the second and third invariant of the stress deviator, and a parameter c which determines the ratio between the yield stresses in uniaxial tension and in pure shear σ_T/τ_Y. For $c = 0$, Drucker yield criterion [11] reduces to the von Mises yield criterion [32] while for $c = 81/66$, the Hershey-Hosford ($m = 6$) yield criterion [19, 22] is recovered. The results obtained with both finite element calculations and linear stability analysis show the same overall trends and there is also quantitative agreement for most of the loading rates considered. In the quasi-static regime, while the specimen elongation when necking occurs is virtually insensitive to the value of the parameter c, both finite element results and analytical calculations using Considère criterion [10] show that the necking strain increases as the parameter c decreases, bringing out the effect of the third invariant of the stress deviator on the formation of quasi-static necks. In contrast, at high initial equivalent strain rates, when the influence of inertia on the necking process becomes important, both finite element simulations and linear stability analysis show that the effect of the third invariant is reversed, notably for long necking wavelengths, with the specimen elongation when necking occurs increasing as the parameter c increases, and the necking strain decreasing as the parameter c decreases.

Keywords:

Necking, Drucker yield criterion, Linear stability analysis, Finite elements, Inertia

---

*Corresponding author. Tel. +34 916249904; Fax: +34 916249430. E-mail address: jarmarti@ing.uc3m.es

1. Introduction

Significant progress has been made over the last few decades in understanding and modeling the formation of dynamic necking instabilities in ductile metallic materials subjected to different stress states, including uniaxial tension, plane strain tension and biaxial tension.

Fressengeas and Molinari [14] derived one-dimensional linear and non-linear solutions to study the influence of inertia and thermal effects on the formation of dynamic necks in bars subjected to simple tension. The linear solutions were obtained using a linear stability analysis, which evaluates the growth of an infinitesimal perturbation superimposed on the homogeneous background solution of the problem at hand: if the perturbation grows faster than the background solution, the plastic flow is unstable and a neck-like deformation field can exist. It was shown that inertia stabilizes long wavelength perturbations, favoring the formation of shorter necks under dynamic loadings. The nonlinear solutions, based on the long wavelength approximation, used a finite differences scheme to solve a two-zone model which included a geometric imperfection in the bar to trigger necking localization. It was shown that inertia/thermal softening delays/promotes necking formation, increasing/decreasing specimen ductility. Few years later, Fressengeas and Molinari [15] extended the three-dimensional linear stability analysis of Hutchinson et al. [23] to include inertia effects and study the formation of necks in metallic sheets modeled with a viscoplastic constitutive relation (no strain-hardening) and subjected to plane strain tension. It was shown that at high strain rates, unlike what happens under quasi-static loadings, the stabilizing effects of stress multiaxiality and inertia on short and long wavelength perturbations promote the growth of an intermediate wavelength (so-called the critical wavelength) for which the growth rate of the perturbation is maximum. This critical wavelength was used by Fressengeas and Molinari [15] to compute the average spacing between necks in the multiple localization patterns that emerge in copper shaped-charge jets, and satisfactory agreement was found between theory and experimental data and nonlinear calculations available in the literature [28, 9]. Few years later, Mercier and Molinari [31] developed a three-dimensional stability analysis to model the formation of multiple necks in dynamically expanded rings. The salient feature of this model was to consider the curvature of the specimens. The plastic behavior of the material was modeled with von Mises yield criterion [32], associated flow rule, and yield stress dependent on strain and strain rate. The predictions for the evolution of the number of necks with the expansion velocity obtained by Mercier and Molinari [31] were compared with the experimental data reported by Altynova et al. [2] for 6061 aluminum rings tested at speeds ranging from 50 m/s to 300 m/s, and reasonable agreement was obtained between experiments and theoretical predictions for the whole range of velocities considered. Moreover, Mercier et al. [30] extended the plane strain linear stability analysis developed by Fressengeas and Molinari [15] to thermoviscoplastic materials with yielding based on the von Mises criterion [32] to predict the critical conditions for the nucleation of necks and the spacing between necks in hemispherical copper and tantalum shells expanded dynamically at strain rates of $\approx 10^4$ s^{-1}. The predictions of the stability analysis for the number of necks were in quantitative agreement with the experiments for both materials tested.

Shenoy and Freund [42] generalized the quasi-static perturbation analysis of the plane tension test developed by Hill and Hutchinson [21] including material inertia to model the nucleation of multiple necks in the ring expansion experiments performed by Niordson [33], Grady and Benson [16] and Altynova et al. [2]. Notice that, unlike the formulation of Mercier and Molinari [31], the model of Shenoy and Freund [42] did not account for the curvature of the specimens. The material behavior was described with the rate-independent hypoelastic constitutive law developed by Stören and Rice [44]. In agreement with Fressengeas and Molinari [15], the results of Shenoy and Freund [42] showed that inertia leads to the development of a critical necking wavelength, which decreases with the strain rate, explaining the experimentally observed increase in the number of necks with the ring expansion velocity (see Niordson [33], Grady and Benson [16] and Altynova et al. [2]). Shortly after, Guduru and Freund [17] adapted the perturbation analysis of Shenoy and Freund [42] to an extending cylinder in order to facilitate direct comparison with the ring expansion experiments of Grady and Benson [16]. Assuming that necking occurs when a critical value of the perturbation growth is reached, Guduru and Freund [17] obtained predictions for the evolution of the number of necks and the necking strain with the expansion velocity. Despite the simplified hypoelastic law used to model the material behavior, the stability analysis results obtained by Guduru and Freund [17] were in reasonable agreement with the experimental data reported by Grady and Benson [16] for OFHC copper and $1100-O$ aluminum rings tested at velocities ranging from 20 m/s to 220 m/s. Guduru and Freund [17] complemented the stability analysis results with finite element calculations to simulate the fragmentation process that followed the formation of multiple necks in the experiments of Grady and Benson [16]. The material behavior was described with an elasto-plastic constitutive model with yielding based on the porous plasticity criterion developed by Gurson [18], Tvergaard [45] and Tvergaard and Needleman [46]. Material fracture was assumed to occur when a critical level of porosity is reached. The finite element predictions of Guduru and Freund [17] were in quantitative agreement with the number of necks and fragments obtained in the experiments performed by Grady and Benson [16] for both OFHC copper and $1100-O$ aluminum rings.

Zhou et al. [55] developed a one-dimensional linear stability analysis which accounts for stress multiaxiality effects on necking formation using Bridgman approximation [4] for the hydrostatic stresses that develop in a necked section. The material was modeled using von Mises plasticity [32] with the yield stress dependent on strain and strain rate. In agreement with Shenoy and Freund [42], the critical necking wavelength was found to decrease with the strain rate and increase with the strain rate sensitivity. Zhou et al. [55] also showed that the strain rate sensitivity slows down the growth of perturbations, stabilizing the material behavior and delaying necking formation. The stability analysis of Zhou et al. [55] was later used by Zaera et al. [51] and Rodríguez-Martínez et al. [41] to study the influence of strain induced martensitic transformation and dynamic recrystallization on the formation of multiple necks in steel and titanium bars subjected to dynamic stretching. The main novelty of the works of Zaera et al. [51] and Rodríguez-Martínez et al. [41] was to incorporate the thermomechanical coupling into the formulation of Zhou et al. [55], including the heat release due to plastic dissipation and the exothermic character of the microstructural evolutions. Shortly after, N'souglo et al. [36] extended the linear stability analysis of Zhou et al. [55] to consider materials with yielding based on Gurson [18] criterion. The predictions for the necking strain and the critical necking wavelength were compared with finite element simulations of long bars subjected to dynamic stretching, and reasonable agreement was found for strain rates ranging from 1000 s^{-1} to 50000 s^{-1}.

Xue et al. [50] developed a non-linear two-zone model based on the long wavelength approximation to describe necking formation and development in metallic plates of 20 mm thickness subjected to plane strain tension. The theoretical predictions were compared with finite element simulations in which the plate was modeled as an array of unit-cells with sinusoidal periodic geometric perturbations. The plastic behavior of the material was described using von Mises criterion [32], with yield stress dependent on strain and strain rate. Two-zone model calculations and finite element computations were performed for strain rates ranging from 100 s^{-1} to 2000 s^{-1}. The two-zone analysis captured the neck retardation due to inertia effects, however, because stress multiaxiality effects were not included in the formulation of the model, short necking wavelengths were not suppressed, and the two-zone analysis failed to predict the emergence of a critical necking wavelength for which the energy required to trigger a neck is minimum. Very recently, Jacques [24] developed a non-linear two-zone model that extends the formulation of Xue et al. [50] to consider any arbitrary in-plane loading and accounts for the hydrostatic stresses which develop inside a necked region using Bridgman approximation [4]. The predictions of the non-linear two-zone model of Jacques [24] for the necking strain were compared with the unit-cell finite element calculations of Rodríguez-Martínez et al. [39], who extended the computational model of Xue et al. [50] to consider loading paths ranging from plane strain to equibiaxial tension. Excellent agreement was found between theoretical model predictions and finite element calculations, for all the loading paths considered, and strain rates ranging from 5000 s^{-1} to 50000 s^{-1}. Moreover, N'souglo et al. [34] have extended the non-linear two-zone model developed by Jacques [24] to consider materials described with the anisotropic yield criterion of Hill [20], and constructed dynamic forming limit diagrams for strain rates ranging from 100 s^{-1} to 50000 s^{-1}. The formability limits at necking obtained with the non-linear two-zone model were compared with unit-cell finite element calculations and with a linear stability analysis specifically developed to model dynamic necking in anisotropic thin plates subjected to biaxial stretching. The study of N'souglo et al. [34] encompassed five different materials, two of them were *model materials* with mechanical properties specifically tailored to bring to light the roles of inertia and orthotropy in dynamic formability, and the other three were actual materials, namely, TRIP-780 steel, AA 5182-O and AA 6016-T4. The results obtained with the three approaches –two-zone model, stability analysis and unit-cell finite element calculations– showed qualitative agreement for the five materials considered, for the whole range of strain rates investigated, and for loading paths ranging from plane strain tension to equibiaxial stretching. Consistent with the quasi-static forming limit diagrams obtained by Sowerby and Duncan [43], Parmar and Mellor [37], Barlat [3] and Butuc et al. [5] using the two-zone approach of Marciniak and Kuczyński [29], N'souglo et al. [34] showed that if inertial effects are considered, just like in the quasi-static case, the influence of the shape of the yield surface on the forming limit strains is small for plane strain stretching while being important for biaxial stretching.

However, notice that most of the papers published so far on dynamic necking instabilities, including those cited above, consider materials governed by a hypoelastic equation (e.g. refs. [42, 17]), or assume that the material behavior in the plastic range obeys either von Mises [32], Gurson [18] or Hill [20] yield criterion (e.g. refs. [17, 31, 50, 26, 27, 36, 34]), and therefore they do not account for the effect of the third invariant of the stress deviator on necking localization. An exception is the recent work of N'souglo et al. [35], who developed a linear stability analysis and performed unit-cell finite element calculations to model the formation of dynamic necks in plates subjected to plane strain tension and made of isotropic ductile materials displaying tension-compression asymmetry. The plastic behavior of the materials was assumed to be governed by the isotropic Cazacu et al. [7] yield criterion, which depends on all principal values of the stress deviator and a unique parameter k. For $k = 0$, the von Mises yield criterion is recovered, otherwise the criterion accounts for strength differential effects, which leads to a specific dependence of yielding on the third invariant of the stress deviator J_3. It was shown that the necking strain and the necking energy are significantly greater for a material that displays a larger flow stress in uniaxial compression than in uniaxial tension ($k < 0$), than for a material modeled with von Mises plasticity. In contrast, the critical necking wavelength was slightly dependent on the tension-compression asymmetry of the material.

In this paper, we study the effect of the third invariant J_3 on the formation of necking instabilities in isotropic metallic materials with no tension-compression asymmetry. Specifically, we develop a linear stability analysis and perform unit-cell finite element calculations to investigate the formation of necking instabilities in elasto-plastic materials with yielding described by the Drucker criterion [11] and subjected to plane strain tension. This isotropic yield criterion is pressure-insensitive, involves the second and third invariant of the stress deviator, and a unique scalar material parameter c (see Section 2). For $c \neq 0$, the criterion accounts for different ratios between the yield stress in uniaxial tension σ_T and the yield stress in pure shear τ_Y, which in turn leads to a very specific dependence of yielding on the third invariant of the stress deviator. If $c = 0$, the Drucker yield criterion reduces to the von Mises yield criterion. It is also worth noting that another widely used isotropic yield criterion for BCC metals, the Hershey-Hosford yield criterion [19, 22] with $m = 6$, is a particular case of Drucker model [11] corresponding to $c = 81/66$ (see the proof in Cazacu et al. [8] and further discussion later in this paper). In Section 3, we present the linear perturbation analysis developed in this paper for materials modeled with Drucker criterion [11]. In Section 4, we present the unit-cell model used in the finite element simulations. Results of the unit-cell calculations conducted using ABAQUS/Standard for low initial equivalent strain rates (10^{-4} s^{-1}) for materials characterized by different values of the parameter c are discussed in Section 5. In Section 6, finite element simulations performed with ABAQUS/Explicit for higher initial equivalent strain rates in the range $400 - 80000$ s^{-1} are compared with the stability analysis predictions. The main conclusions of this investigation are summarized in Section 7.

2. Constitutive framework

We begin with the presentation of the general equations governing elastic/plastic behavior for an isotropic material with isotropic hardening (Section 2.1). Next, we briefly review the Drucker's yield criterion. As previously mentioned, to investigate the influence of J_3 on the plastic behavior and neck formation for both quasi-static and dynamic conditions, theoretical and finite element analyses are presented for materials characterized by different values of the parameter c, describing the J_3 influence. The materials studied and key differences in their yielding behavior are discussed (see Section 2.2). In addition, we show that for plane strain tension, it is possible to obtain the plastic dissipation in closed form even for the case when yielding depends on J_3 (see Section 2.3).

2.1. General equations for elastic/plastic materials

We assume the additive decomposition of the total rate of deformation tensor $\boldsymbol{d}$ into an elastic part $\boldsymbol{d}^e$ and a plastic part $\boldsymbol{d}^p$:

$$\boldsymbol{d} = \boldsymbol{d}^e + \boldsymbol{d}^p \tag{1}$$

where the elastic part of the rate of deformation tensor is related to the rate of the stress by the following linear elastic law:

$$\overset{\triangledown}{\boldsymbol{\sigma}} = \boldsymbol{C} : \boldsymbol{d}^e \tag{2}$$

with $\overset{\triangledown}{\boldsymbol{\sigma}}$ being an objective derivative of the Cauchy stress tensor, which corresponds to the Jaumann derivative in ABAQUS/Standard and to the Green-Naghdi derivative in ABAQUS/Explicit, and $\boldsymbol{C}$ being the fourth-order isotropic elastic tensor defined as:

$$\boldsymbol{C} = 2G\boldsymbol{I}' + K\mathbf{1} \otimes \mathbf{1} \tag{3}$$

where $\mathbf{1}$ is the unit second-order tensor, and $\boldsymbol{I}'$ the unit deviatoric fourth-order tensor. Moreover G and K are the shear and bulk modulus, respectively.

Moreover, the yield condition is expressed as:

$$f = \bar{\sigma} - \sigma_T = 0 \tag{4}$$

where $\bar{\sigma}$ is the equivalent stress associated to the Drucker yield criterion [11] (see equation (13)) and σ_T is the yield stress in uniaxial tension which evolves with the equivalent plastic strain $\bar{\varepsilon}^p$ following a power-law type hardening rule:

$$\sigma_T = \sigma_0 \left(\varepsilon_0 + \bar{\varepsilon}^p\right)^n \tag{5}$$

where σ_0, ε_0, and n are material parameters.

The equivalent plastic strain is defined as:

$$\bar{\varepsilon}^p = \int_0^t \dot{\bar{\varepsilon}}^p d\tau \tag{6}$$

with $\dot{\bar{\varepsilon}}^p$ being the equivalent plastic strain rate. Note that a superposed dot denotes differentiation with respect to time.

Moreover, assuming an associated plastic flow rule, the plastic part of the rate of deformation tensor is:

$$\boldsymbol{d}^p = \dot{\lambda}\frac{\partial \bar{\sigma}}{\partial \boldsymbol{\sigma}} \tag{7}$$

where $\dot{\lambda}$ is the rate of plastic multiplier.

Therefore, the work conjugacy relation:

$$\boldsymbol{\sigma} : \boldsymbol{d}^p = \bar{\sigma}\dot{\bar{\varepsilon}}^p \tag{8}$$

leads to the identity:

$$\dot{\bar{\varepsilon}}^p = \dot{\lambda} \tag{9}$$

2.2. Drucker isotropic yield criterion [11] and materials studied

According to the isotropic Drucker yield criterion [11], yielding is described as:

$$\phi\left(\boldsymbol{\sigma}\right) = J_2^3 - cJ_3^2 \tag{10}$$

where c is a material parameter, and $J_2 = \dfrac{1}{2}\left(s_1^2 + s_2^2 + s_3^2\right)$ and $J_3 = s_1 s_2 s_3$ are, respectively, the second and third invariant of the deviator of the Cauchy stress tensor, defined as $\mathbf{s} = \boldsymbol{\sigma} - \frac{1}{3}\mathrm{tr}(\boldsymbol{\sigma})\mathbf{1}$, where tr denotes the trace operator. Moreover, s_1, s_2 and s_3 are the principal values of the stress deviator $\mathbf{s}$. For the yield function to be convex, the parameter c should belong to the following range: $-27/8 \leq c \leq 2.25$ (for proof, see Cazacu et al. [8]). Note that the parameter c is expressible only in terms of the ratio between the yield stresses in uniaxial tension, σ_T, and pure shear, τ_Y, as:

$$c = \frac{27}{4}\left[1 - \left(\frac{\sqrt{3}\tau_Y}{\sigma_T}\right)^6\right] \tag{11}$$

Remark: It is worth noting that according to the von Mises yield criterion [32], irrespective of the material, the ratio between the yield stresses in uniaxial tension and pure shear is the same, i.e. $\sigma_T/\tau_Y = \sqrt{3}$. In contrast, Drucker criterion [11] allows to differentiate between isotropic materials. Namely, for materials with $\dfrac{\sigma_T}{\tau_Y} > \sqrt{3}$ the parameter c is positive, while for a material with $\dfrac{\sigma_T}{\tau_Y} < \sqrt{3}$, the parameter c is negative. Note that for $c = 0$, the von Mises yield criterion is recovered. It is also worth mentioning that very recently it was demonstrated that the Hershey-Hosford yield criterion [19, 22] for isotropic BCC materials can be expressed in a very simple polynomial form in terms of the second and third invariant of the stress deviator, as follows (see Cazacu [6] and Cazacu et al. [8]):

$$\phi_{BCC}(\boldsymbol{\sigma}) = (s_1 - s_2)^6 + (s_2 - s_3)^6 + (s_3 - s_1)^6 = 66J_2^3 - 81J_3^2 \tag{12}$$

which means that the Hershey-Hosford yield criterion [19, 22] for isotropic BCC materials is a particular case of Drucker [11] corresponding to $c = 81/66$.

The equivalent stress associated to the Drucker yield criterion [11] is:

$$\bar{\sigma} = \frac{\sqrt{3}}{\left(1 - \dfrac{4c}{27}\right)^{1/6}}\left(J_2^3 - cJ_3^2\right)^{1/6} \tag{13}$$

2.2.1. Materials studied

The main objective of this investigation is to study the influence of the third invariant of the stress deviator on the formation of necking instabilities in isotropic metal sheets with the same response in tension and compression when subjected to plane strain extension. To this end, linear stability analysis and finite element calculations will be performed for Drucker materials with the same elastic behavior, initial yield stress and hardening in uniaxial tension but characterized by different values of the parameter c. The numerical values of the elastic moduli and hardening parameters in equations (3) and (5), are given in Table 1. Specifically, we analyze the inception of necking instabilities in a material with $\sigma_T/\tau_Y < \sqrt{3}$ in comparison with a von Mises material ($c = 0$) and materials with $\sigma_T/\tau_Y > \sqrt{3}$ (i.e. $c > 0$).

To facilitate the discussion of the results, we denote as:

- Material 1: the von Mises material for which $c = 0$ and $\sigma_T/\tau_Y = \sqrt{3}$.
- Material 2: it is characterized by $\sigma_T/\tau_Y < \sqrt{3}$ and $c = -1.5$, may be representative of certain aluminum alloys.
- Material 3: it is characterized by $\sigma_T/\tau_Y > \sqrt{3}$ and $c = 81/66$. This is representative of an isotropic BCC material obeying Hershey-Hosford [19, 22] yield criterion, see equation (12).
- Material 4: it is characterized by $c = 2.25$, which corresponds to the highest σ_T/τ_Y ratio that can be accommodated by the Drucker yield criterion [11] (i.e. maximum value of c for which the yield function given by Eq. (10) is convex).

Fig. 1 shows the projection of the yield loci of these materials in the biaxial plane (i.e. plane corresponding to one of the eigenvalues of the Cauchy stress tensor being equal to zero). We only show the tension-tension quadrant because according to Drucker [11] the yielding response is the same in tension and compression. Note that, since the Material 2 is characterized by a negative value of c, its yield locus is exterior to the von Mises ellipse ($c = 0$). On the other hand, the yield loci of Material 3 and Material 4, which are characterized by positive values of c, are interior to the von Mises ellipse.

2.3. Effect of the third-invariant on the plastic dissipation according to Drucker yield criterion [11]

A key step in the stability analysis calculations is to obtain the plastic dissipation or equivalent plastic strain rate, which allows to derive the fundamental solution of the problem to be perturbed, see Section 3. Indeed, it

Symbol	Property and units	Value
ρ_0	Initial density (kg/m^3)	7800
G	Elastic shear modulus (GPa), Eq. (3)	115.4
K	Bulk modulus (GPa), Eq. (3)	250
σ_0	Material parameter (GPa), Eq. (5)	1.8
ε_0	Material parameter, Eq. (5)	0.0027
n	Material parameter, Eq. (5)	0.1

Table 1: *Numerical values of initial density, elastic constants and hardening parameters. Data after N'souglo et al. [35].*

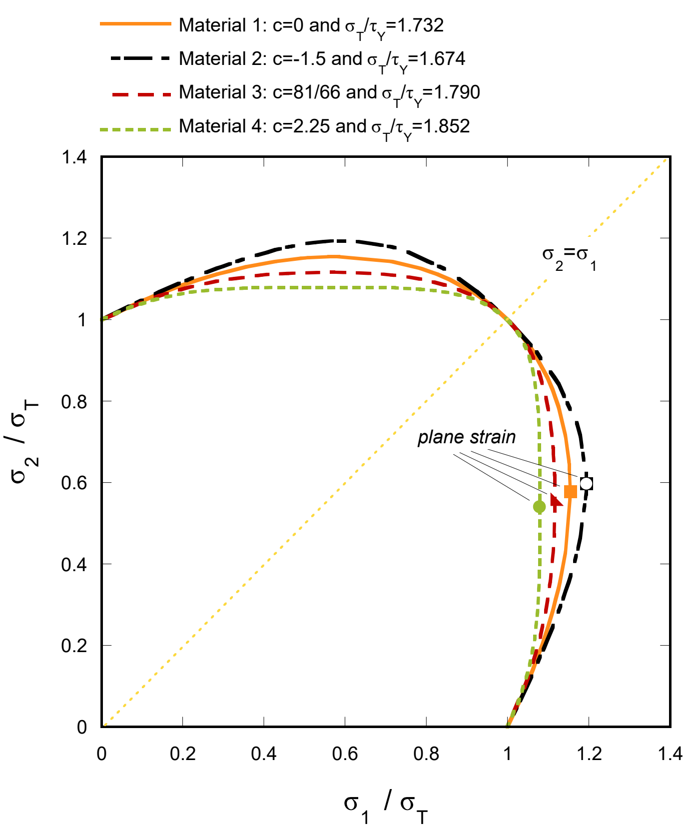

Figure 1: Plane stress ($\sigma_3 = 0$) yield loci according to the isotropic Drucker yield criterion [11], Eq. (10), for Material 1 (von Mises material, $c = 0$ and $\sigma_T/\tau_Y = \sqrt{3}$), Material 2 ($c = -1.5$ and $\sigma_T/\tau_Y = 1.674$), Material 3 (Hershey-Hosford for a BCC material, $c = 81/66$ and $\sigma_T/\tau_Y = 1.790$) and Material 4 ($c = 2.25$ and $\sigma_T/\tau_Y = 1.852$). The tensile plane strain points are represented by symbols.

is well known that for non-quadratic yield criteria involving J_3, for general loadings, the equivalent plastic strain rate cannot be obtained in closed form. However, for plane strain tension, this is feasible, as it is shown below.

To simplify writing hereafter, we will denote the plastic strain rate tensor and the equivalent plastic strain rate by $\boldsymbol{d}$ and $\dot{\bar{\varepsilon}}$, respectively. Note that this notation is consistent with the fact that we neglect elasticity in the linear stability analysis (see Section 3.2). For a material obeying Drucker yield criterion [11] and associated flow rule:

$$\boldsymbol{d} = \dot{\lambda}\left[3J_2^2\boldsymbol{s} - 2cJ_3\left(\boldsymbol{s}^2 - \frac{2}{3}J_2\mathbf{1}\right)\right]\frac{A}{6}\bar{\sigma}^{-5} \tag{14}$$

$$\frac{\mathrm{tr}\,(\boldsymbol{d}^2)}{2} = \dot{\lambda}^2\bar{\sigma}^{-10}\left(\frac{A}{6}\right)^2\left[9J_2^3 + \left(\frac{4c^2}{3} - 18c\right)J_3^2\right]J_2^2 \tag{15}$$

where $A = \dfrac{27^2}{27-4c}$. For the problem studied, i.e. thin plates under plane strain stretching, relative to the Cartesian coordinate system given in Fig. 2, $d_{zz} = 0$ and $\sigma_{yy} = 0$. Therefore, the principal values of the plastic strain rate tensor are:

$$d_1 = d_{xx} > 0, \quad d_2 = d_{zz} = 0, \quad d_3 = -d_1 = d_{yy} < 0 \tag{16}$$

Further making use of Eq. (14), we obtain that:

$$s_2\left[\frac{3}{4}\left(s_1^2 + s_2^2 + s_3^2\right)^2 - \frac{2c}{3}\left(-s_1^2 + 2s_2^2 - s_3^2\right)s_1 s_3\right] = 0 \tag{17}$$

This leads to:

$$s_2 = 0 \tag{18}$$

or

$$9\left(s_1^2+s_2^2+s_3^2\right)^2-8c\left(-s_1^2+2s_2^2-s_3^2\right)s_1s_3=0 \quad (19)$$

Since $\sigma_{yy}=0$, Eq. (19) reduces to the following algebraic equation for $b=\sigma_{zz}/\sigma_{xx}$:

$$(4c-27)\,b^4+(54-8c)\,b^3+(-6c-81)\,b^2+(10c+54)\,b+(4c-27)=0 \quad (20)$$

For $-27/8\leq c\leq 2.25$, which is the range of the parameter c for which the Drucker yield surface is convex, the above equation has no real solution. Consequently, $d_2=0$ leads to $s_2=0$. It follows that the state of stress is such that $J_3=0$, $J_2=s_{xx}^2$ and $\bar{\sigma}=A^{1/6}s_{xx}$. Further substitution into Eq. (14) leads to:

$$\dot{\bar{\varepsilon}}=\frac{2}{A^{1/6}}d_{xx}=\dot{\bar{\varepsilon}}_{\mathrm{Mises}}\left(1-\frac{4c}{27}\right)^{1/6} \quad (21)$$

where d_{xx} is the strain rate in the loading direction. The above expression shows that for materials with $c<0$, $\dot{\bar{\varepsilon}}>\dot{\bar{\varepsilon}}_{\mathrm{Mises}}$, while for materials with $c>0$, $\dot{\bar{\varepsilon}}<\dot{\bar{\varepsilon}}_{\mathrm{Mises}}$. This difference in equivalent plastic strain rate and consequently on plastic dissipation as compared to a von Mises material ($c=0$) leads to different localization behaviors for both quasi-static and dynamic loadings (see Sections 5 and 6).

3. Statement of the problem and theoretical model

The statement of the problem is general. We use the notations customarily considered (e.g. see N'souglo et al. [35]). We analyze a thin plate of initial thickness h^0 and initial length L^0, see Fig. 2. Cartesian coordinates (X,Y,Z) mark the location of a material point in the undeformed state, while the location of the same material point in the deformed state is (x,y,z). The plate is under plane strain constraint in the out-of-plane direction Z, and the through-thickness direction Y is assumed of plane stress. Constant and opposed stretching velocities $\pm V_x$ are applied at the ends of the plate $X=\pm\frac{L^0}{2}$, as shown in Fig. 2. As anticipated in Section 2.3, we neglect the elastic deformations and $\bar{\varepsilon}=\bar{\varepsilon}^p$ will be named hereafter equivalent strain and $\dot{\bar{\varepsilon}}=\dot{\bar{\varepsilon}}^p$ equivalent strain rate. The kinematics of the problem can be found in Appendix A of N'souglo et al. [35]. We present the equations governing the homogeneous deformation in Section 3.1, and the main features of the linear stability analysis in Section 3.2.

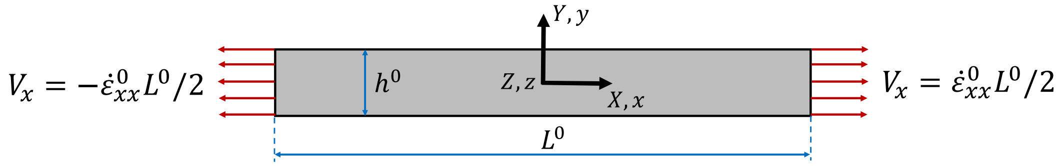

Figure 2: Schematic representation of the geometry and boundary conditions of the problem addressed: a plate of initial thickness h^0 and initial length L^0 stretched at constant velocity V_x. The specimen is under plane strain constraint in the out-of-plane direction Z, and the direction Y is assumed of plane stress. This figure is taken from N'souglo et al. [35].

3.1. Governing equations

The equations governing the problem are:

$$
\begin{cases}
d_{xx} = \dfrac{\partial V_x}{\partial x} & \text{(22a)} \\
F_{xx} = \dfrac{\dot{F}_{xx}}{d_{xx}} & \text{(22b)} \\
F_{xx} F_{yy} = 1 & \text{(22c)} \\
h = h^0 F_{yy} & \text{(22d)} \\
\dfrac{\partial \left(h \sigma_{xx}^{avg} \right)}{\partial X} = \rho h^0 \dfrac{\partial V_x}{\partial t} & \text{(22e)} \\
\sigma_{xx}^{avg} = \left(\sqrt{1 + \phi^{-1}} \ln \left(1 + 2\phi + 2\sqrt{\phi(1+\phi)} \right) - 1 \right) \sigma_{xx} & \text{(22f)} \\
d_{xx} = \dot{\bar{\varepsilon}} \dfrac{\partial \bar{\sigma}}{\partial \sigma_{xx}} & \text{(22g)} \\
d_{zz} = \dot{\bar{\varepsilon}} \dfrac{\partial \bar{\sigma}}{\partial \sigma_{zz}} = 0 & \text{(22h)}
\end{cases}
$$

where expressions (22a) and (22b) are kinematic relations, equation (22c) is the incompressibility condition, the continuity equation is given by expression (22d), equation (22e) is the balance of linear momentum in Lagrangian description, relation (22f) gives the average stress in the loading direction, and the flow rule is given by equations (22g) and (22h). In this set of equations, V_x is the imposed velocity in the loading direction (as mentioned before), d_{xx} and d_{zz} are the strain rates in the loading and the out-of-plane directions, respectively, F_{xx} and F_{yy} are the deformation gradients in the loading and the through-thickness directions, h is the current thickness of the plate, ρ is the material density (assumed constant), σ_{xx} and σ_{zz} are the uniform stresses in the loading and the out-of-plane directions, respectively, σ_{xx}^{avg} is the average stress in the loading direction [35] and $\phi = \dfrac{h}{8} \dfrac{\partial^2 h}{\partial x^2}$ is the argument of the Bridgman correction factor [4] which accounts for the axial hydrostatic stress that develops in a necked zone (see Walsh [48] and Zhou et al. [55]). Note that equations (22g)-(22h) need to be specialized for the specific yielding behavior considered.

Remark: The key novelty of this paper is to extend the theoretical analysis developed in N'souglo et al. [35] to Drucker's criterion [11]. Namely, specialization to a given plastic constitutive behavior is performed by completing the system of governing equations (22) with the yield condition, the yield stress in uniaxial tension, the equivalent strain and the equivalent stress; for the case of the isotropic Drucker yield criterion, see equations (4)-(6) and (13).

The initial and boundary conditions are:

$$\begin{aligned} &V_x(X,Y,0) = \dot{\varepsilon}^0_{xx} X; \qquad &\sigma_{ij}(X,Y,0) = 0 \\ &\bar{\varepsilon}(X,Y,0) = 0; \qquad &h(X,Y,0) = h^0 \end{aligned} \tag{23}$$

$$V_x(L^0/2, Y, t) = -V_x(-L^0/2, Y, t) = \dot{\varepsilon}^0_{xx} L^0/2 \tag{24}$$

where $\dot{\varepsilon}^0_{xx}$ is the initial strain rate in the loading direction.

Remark: note that the applied loading is selected through the input value of the initial equivalent strain rate $\dot{\bar{\varepsilon}}^0$. The rationale is that the equivalent strain rate enters into the nondimensionalization of the set of algebraic equations resulting from the linear stability analysis, thus controlling the value of the inertia parameter (parameter $\tilde{L}^{-1}$, see Eq. (31)). On the other hand, while the same rationale has been employed by other authors, e.g. Zaera et al. [52] and N'souglo et al. [35], we are aware that it is also customary in the literature to impose the stretch rate as the loading condition [49, 34], since it may bear closer resemblance to the actual boundary conditions in dynamic experiments like the expansion of hemispherical shells (see Mercier et al. [30]). Hence, stability analysis results and finite element calculations obtained imposing the stretching rate, namely $\dot{\varepsilon}^0_{xx} = 4000\ \mathrm{s}^{-1}$ and $\dot{\varepsilon}^0_{xx} = 80000\ \mathrm{s}^{-1}$, are reported in Appendix A. On the other hand, for the case when yielding is described by the Drucker yield criterion [11], according to equation (21), the relation between $\dot{\bar{\varepsilon}}^0$ and $\dot{\varepsilon}^0_{xx}$ for plane strain tension is:

$$\dot{\bar{\varepsilon}}^0 = \frac{2}{A^{1/6}}\dot{\varepsilon}^0_{xx} \tag{25}$$

Note that, for a given value of $\dot{\bar{\varepsilon}}^0$, as the parameter c increases (recall that $A = \frac{27^2}{27-4c}$), i.e. as the ratio σ_T/τ_Y increases (see equation (11)), $\dot{\varepsilon}^0_{xx}$ increases.

The solution of the problem at any given loading time, also called homogeneous or fundamental solution, is:

$$\mathbb{S}^1 = (V^1_x, d^1_{xx}, F^1_{xx}, F^1_{yy}, h^1, \bar{\varepsilon}^1, \dot{\bar{\varepsilon}}^1, \sigma^1_{xx}, \sigma^1_{zz}, \sigma^{avg,1}_{xx}, \bar{\sigma}^1, \sigma^1_T, \phi^1)^T \tag{26}$$

3.2. Linear stability analysis for an isotropic material with yielding according to Drucker criterion [11]

The stability of the fundamental solution is tested by introducing at some time t^1 a small perturbation $\delta\mathbb{S}$ of the form:

$$\delta\mathbb{S}(X,t)_{t^1} = \delta\mathbb{S}^1 e^{i\xi X + \eta(t-t^1)} \tag{27}$$

with

$$\delta\mathbb{S}^1 = (\delta V_x, \delta d_{xx}, \delta F_{xx}, \delta F_{yy}, \delta h, \delta\bar{\varepsilon}, \delta\dot{\bar{\varepsilon}}, \delta\sigma_{xx}, \delta\sigma_{zz}, \delta\sigma^{avg}_{xx}, \delta\bar{\sigma}, \delta\sigma_T, \delta\phi)^T \tag{28}$$

where $\delta\mathbb{S}^1$ is the perturbation amplitude, ξ is the wavenumber and η is the growth rate of the perturbation at time t^1. Note that η is usually referred to as the instantaneous instability index. Here ξ and η are considered time independent (frozen coefficients method), however, note that a time dependent numerical solution has been recently developed by Xavier et al. [49] for von Mises materials subjected to plane strain tension. The perturbation, Eq. (27), is imposed on lines $X = \textit{constant}$ because the preferential neck orientation for isotropic materials subjected to plane strain tension is perpendicular to the loading direction (i.e. it corresponds to the direction of zero extension, see refs. [30], [39] and [24]).

Therefore, the perturbed solution is given by:

$$\mathbb{S} = \mathbb{S}^1 + \delta\mathbb{S} \tag{29}$$

with $|\delta\mathbb{S}| \ll |\mathbb{S}^1|$. A system of linear algebraic equations is obtained by substituting equation Eq. (29) into the governing equations (22) specialized for Drucker yield criterion [11] and keeping only the first-order terms in the increments $\delta\mathbb{S}^1$. This system of equations, which is not explicitly shown in this paper for the sake of brevity, has been adimensionalized by introducing the following dimensionless groups:

$$\begin{array}{lllll}
\hat{V}_x = \dfrac{V_x}{h^0\dot{\bar{\varepsilon}}^1}; & \hat{d}_{xx} = \dfrac{d_{xx}}{\dot{\bar{\varepsilon}}^1}; & \hat{F}_{xx} = F_{xx}; & \hat{F}_{yy} = F_{yy}; & \hat{h} = \dfrac{h}{h^0}; \\
\hat{\bar{\varepsilon}} = \bar{\varepsilon}; & \hat{\dot{\bar{\varepsilon}}} = \dfrac{\dot{\bar{\varepsilon}}}{\dot{\bar{\varepsilon}}^1}; & \hat{\sigma}_{xx} = \dfrac{\sigma_{xx}}{\sigma_0}; & \hat{\sigma}_{zz} = \dfrac{\sigma_{zz}}{\sigma_0}; & \hat{\sigma}_{xx}^{avg} = \dfrac{\sigma_{xx}^{avg}}{\sigma_0}; \\
\hat{\bar{\sigma}} = \dfrac{\bar{\sigma}}{\sigma_0}; & \hat{\sigma}_T = \dfrac{\sigma_T}{\sigma_0}; & \hat{\phi} = \phi; & \hat{\eta} = \dfrac{\eta}{\dot{\bar{\varepsilon}}^1}; & \hat{\xi} = \xi h^0
\end{array}$$

A non-trivial solution for $\delta\mathbb{S}^1$ is obtained only if the determinant of the matrix of coefficients of the system of adimensionalized linear algebraic equations is equal to zero. This condition leads to the following cubic algebraic equation for the growth rate of the perturbation $\hat{\eta}$:

$$B_3(\mathbb{S}^1)\hat{\eta}^3 + B_2(\mathbb{S}^1)\hat{\eta}^2 + B_1(\mathbb{S}^1, \hat{\xi})\hat{\eta} + B_0(\mathbb{S}^1, \hat{\xi}) = 0 \tag{30}$$

with

$$\begin{aligned}
B_3(\mathbb{S}^1) &= 8\hat{M}_2 \left(\hat{d}_{xx}^1\right)^2 \left(\hat{F}_{xx}^1\right)^3 \\
B_2(\mathbb{S}^1) &= 8\hat{Q} \left(\hat{F}_{xx}^1\right)^3 \left(\hat{M}_2\hat{R}_1 - \hat{M}_1\hat{R}_2\right) \\
B_1(\mathbb{S}^1, \hat{\xi}) &= \frac{2}{3}\hat{h}^1\hat{M}_2\left(\tilde{L}\hat{\xi}\right)^2 \left(\left(\hat{d}_{xx}^1\hat{h}^1\hat{\xi}\right)^2 \hat{\sigma}_{xx}^1 + 12\left(\hat{F}_{xx}^1\right)^2\left(\hat{Q} - \left(\hat{d}_{xx}^1\right)^2\hat{\sigma}_{xx}^1\right)\right) \\
B_0(\mathbb{S}^1, \hat{\xi}) &= \frac{2}{3}\hat{h}^1\hat{Q}\left(\tilde{L}\hat{\xi}\right)^2 \left(-12\hat{M}_2\hat{d}_{xx}^1\left(\hat{F}_{xx}^1\right)^2 - \hat{\sigma}_{xx}^1\left(\hat{M}_2\hat{R}_1 - \hat{M}_1\hat{R}_2\right)\left(12\left(\hat{F}_{xx}^1\right)^2 - \left(\hat{h}^1\hat{\xi}\right)^2\right)\right)
\end{aligned} \tag{31}$$

where $\frac{1}{\tilde{L}^2} = \frac{\rho\left(h^0\dot{\bar{\varepsilon}}^1\right)^2}{\sigma_0}$ represents the inertial resistance to motion, $\hat{M}_1 = \frac{\sigma_0}{\dot{\bar{\varepsilon}}^1}\frac{\partial d_{zz}}{\partial\sigma_{xx}}\Big|_{t^1}$ and $\hat{M}_2 = \frac{\sigma_0}{\dot{\bar{\varepsilon}}^1}\frac{\partial d_{zz}}{\partial\sigma_{zz}}\Big|_{t^1}$ are the non-dimensional derivatives of d_{zz} with respect to the components of the Cauchy stress tensor, $\hat{R}_1 = \frac{\sigma_0}{\dot{\bar{\varepsilon}}^1} \frac{\partial d_{xx}}{\partial \sigma_{xx}}\Big|_{t^1}$ and $\hat{R}_2 = \frac{\sigma_0}{\dot{\bar{\varepsilon}}^1} \frac{\partial d_{xx}}{\partial \sigma_{zz}}\Big|_{t^1}$ are the non-dimensional derivatives of d_{xx} with respect to the components of the Cauchy stress tensor and $\hat{Q} = \frac{1}{\sigma_0} \frac{\partial \sigma_T}{\partial \bar{\varepsilon}}\Big|_{t^1}$ is the non-dimensional strain sensitivity of the material.

Equation (30) gives, for a certain value of the loading time t^1, the value of the dimensionless instantaneous instability index $\hat{\eta}$ as a function of the dimensionless wavenumber $\hat{\xi}$. Note also that the dimensionless wavenumber is related to the normalized perturbation wavelength L^0/h^0 as: $L^0/h^0 = \dfrac{2\pi}{\hat{\xi}}$. The value of $\hat{\eta}$ is an indicator of the instantaneous stability of the solution. Equation (30) has only one real root, which is the physical solution of the problem. The requisite for unstable growth of the perturbation is given by the real part of $\hat{\eta}$, denoted $\mathrm{Re}(\hat{\eta})$, to be positive $\hat{\eta}^+$. Thus, if $\mathrm{Re}(\hat{\eta}) > 0$ a neck-like deformation field can exist. The stabilizing effect of inertia and stress multiaxiality on small and large wavenumbers, respectively, boosts the growth of a finite number of intermediate modes. The mode with the greatest value of the instantaneous instability index $\hat{\eta}^+$ is characterized by a wavenumber that is referred to as the critical instantaneous wavenumber, the critical instantaneous necking mode, or the critical instantaneous perturbation mode $\hat{\xi}_c^{\hat{\eta}^+}$. The critical instantaneous wavenumber, which evolves with the loading time, and thus with the strain in the material, can be used to calculate the critical instantaneous perturbation wavelength $\left(L^0/h^0\right)_c^{\hat{\eta}^+}$ (see Figs. 6 and 7 in Section 6.2). Moreover, an alternative indicator of the stability of the solution was proposed by Fressengeas and Molinari [15], who used a cumulative instability index, $I = \int_0^t \hat{\eta}^+ \dot{\bar{\varepsilon}}^1 dt$ to track the evolution of the instantaneous growth rate of all the growing modes (see also Petit et al. [38] and El Maï et al. [13]). To calculate I, we introduce the perturbation at different times and sum the instantaneous growth rate obtained for each loading time [35]. The mode with the greatest value of the cumulative instability index I is called the critical cumulative wavenumber, the critical cumulative necking mode, or the critical cumulative perturbation mode $\hat{\xi}_c^I$. Like the critical instantaneous wavenumber, $\hat{\xi}_c^I$ also evolves with the loading time, i.e. with the strain, and it can be used to calculate the critical cumulative perturbation wavelength $\left(L^0/h^0\right)_c^I$ (see Figs. 6 and 7 in Section 6.2 and Fig. 16 in Section 6.3).

4. Unit-cell finite element model

This section presents the 2D finite element model developed in ABAQUS [1] to simulate necking localization in Drucker [11] materials subjected to plane strain tension. Material points are referred to using a Cartesian coordinate system with positions in the reference configuration denoted as (X, Y). The origin of coordinates is located in the center of mass of the specimen, see Fig. 3. We use the same finite element model as N'souglo et al. [35] who, following the earlier work of Xue et al. [50], modeled a plate subjected to plane strain tension and with geometrical periodic perturbations as an array of unit-cells with sinusoidal spatial imperfections given by the following expression:

$$h = h^0 - \delta\left[1 + \cos\left(\frac{2\pi X}{L^0}\right)\right] \tag{32}$$

where h is the perturbed thickness of the unit-cell and δ is the amplitude of the imperfection. Consistent with the notation used in the theoretical model presented in Section 3, L^0 and h^0 are the initial length and the unperturbed thickness of the unit-cell, respectively. Due to the symmetry of the problem, only a quarter of the unit-cell is analyzed, see Fig. 3. Finite element simulations will be conducted for several normalized cell lengths varying within the range $0.5 \leq \frac{L^0}{h^0} \leq 6$, with $\Delta = \frac{2\delta}{h^0} = 0.2\%$ and $h^0 = 2$ mm. The normalized cell length is the counterpart of the normalized perturbation wavelength in the linear stability analysis, see Section 3.2, and it will be also denoted as L^0/h^0. Hereinafter, the normalized cell length will be also referred to as cell size. Note that the spatial imperfection is imposed on lines $X = constant$ (see Section 3.2). The initial and boundary conditions used in the finite element model are consistent with those used in the theoretical model (see Section 3.1 and Fig. 3).

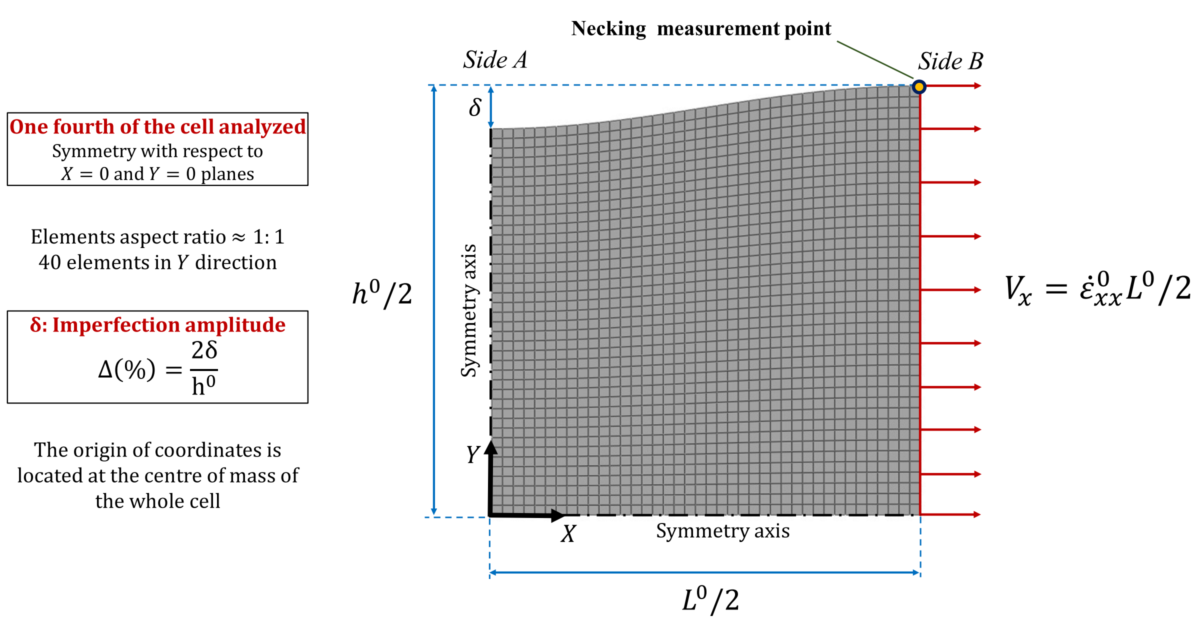

Figure 3: Finite element model. Mesh and boundary conditions. A large imperfection amplitude has been shown in the figure for better illustration of the geometric perturbation. This figure is taken from N'souglo et al. [35].

The finite element model is meshed with four-node bilinear plane strain elements with reduced integration and hourglass control (CPE4R in ABAQUS notation), with initial dimensions $\approx 25 \times 25\ \mu\mathrm{m}^2$. The constitutive model presented in Section 2 has been implemented in ABAQUS [1] through UMAT and VUMAT user subroutines. The UMAT has been used to obtain the low strain rate finite element results, $\dot{\bar{\varepsilon}}^0 = 10^{-4}\ \mathrm{s}^{-1}$, reported in Figs. 4, 5 and 15, and the VUMAT has been used to obtain all the other finite element calculations reported in this paper for higher strain rates. The integration of the constitutive equations in both UMAT and VUMAT subroutines has been performed using fully implicit algorithms.

5. Effect of the third invariant on the formation of quasi-static necks in materials with the same response in tension and compression and yielding according to Drucker criterion [11]

This section presents analytical calculations based on Considère criterion [10] and finite element results which bring to light the influence of the third invariant J_3 described by the parameter c, on the formation of quasi-static necks under plane strain stretching. Results are shown for Material 1 (von Mises material, $c = 0$ and $\sigma_T/\tau_Y = \sqrt{3}$), Material 2 ($c = -1.5$ and $\sigma_T/\tau_Y = 1.674$), Material 3 (Hershey-Hosford for a BCC material, $c = 81/66$ and $\sigma_T/\tau_Y = 1.790$) and Material 4 ($c = 2.25$ and $\sigma_T/\tau_Y = 1.852$), see Section 2.2. Recall the relationship between the parameter c and the ratio σ_T/τ_Y, Eq. (11), which shows that σ_T/τ_Y increases with c.

5.1. Analytical calculations based on Considère criterion

For plane strain tension, according to the Considère criterion [10], the onset of instability occurs when the axial force in the specimen attains its maximum value. Making use of Eqs. (6), (13) and (21), we obtain the following expressions for the necking strain $\bar{\varepsilon}^{neck}$ and the necking stretch F_{xx}^{neck} (i.e. the equivalent strain and the axial stretch corresponding to the onset of necking):

$$\bar{\varepsilon}^{neck} = \frac{2n}{A^{1/6}} - \varepsilon_0 \tag{33}$$

$$F_{xx}^{neck} = e^{\frac{A^{1/6}}{2}\bar{\varepsilon}^{neck}} \tag{34}$$

relations which are used to obtain the results presented in Table 2 for the materials studied. Note that both the necking strain $\bar{\varepsilon}^{neck}$ and the necking stretch F_{xx}^{neck} increase as the value of c decreases (i.e. as the ratio between the yield stresses in uniaxial tension and in pure shear decreases). However, while the value of $\bar{\varepsilon}^{neck}$ is 10% greater in the case of $\sigma_T/\tau_Y = 1.674$ than in the case of $\sigma_T/\tau_Y = 1.852$ (these are the minimum and maximum values considered for σ_T/τ_Y), the variations in the necking stretch F_{xx}^{neck} with c only appear in the fourth decimal digit. This is an original result of this investigation that, to the authors' knowledge, has not been reported before.

Material	**Necking strain**	**Necking stretch**
Material 1: von Mises material, $c = 0$ and $\sigma_T/\tau_Y = \sqrt{3}$	0.1127	1.1025
Material 2: $c = -1.5$ and $\sigma_T/\tau_Y = 1.674$	0.1166	1.1026
Material 3: $c = 81/66$ and $\sigma_T/\tau_Y = 1.790$	0.1089	1.1025
Material 4: $c = 2.25$ and $\sigma_T/\tau_Y = 1.852$	0.1052	1.1024

Table 2: Necking strain and necking stretch calculated for Material 1 (von Mises material, $c = 0$ and $\sigma_T/\tau_Y = 1.732$), Material 2 ($c = -1.5$ and $\sigma_T/\tau_Y = 1.674$), Material 3 ($c = 81/66$ and $\sigma_T/\tau_Y = 1.790$) and Material 4 ($c = 2.25$ and $\sigma_T/\tau_Y = 1.852$) using Considère criterion, equations (33) and (34).

Note that the Considère criterion [10] only provides reliable quantitative predictions for the necking strain and the necking stretch in smooth specimens subjected to quasi-static loading conditions. If inertia effects are important, the necking localization occurs for equivalent strains and axial stretches greater than the ones reported in Table 2, as it will be shown in Section 6. Moreover, for notched specimens, the hydrostatic stresses that develop inside the notch also delay necking localization, as it will be discussed below.

5.2. Unit-cell finite element calculations

The finite element simulations are performed in ABAQUS/Standard at a low initial equivalent strain rate, $\dot{\bar{\varepsilon}}^0 = 10^{-4}$ s^{-1}. Inertia effects are not considered in the calculations. Recall that the normalized amplitude of the imperfection is $\Delta = 0.2\%$ in all the finite element computations reported in this paper.

Fig. 4 shows the evolution of the equivalent strain $\bar{\varepsilon}$ with the axial stretch F_{xx} for two different cell sizes, $L^0/h^0 = 1$ and $L^0/h^0 = 3.5$, and the various materials investigated in this paper. The axial stretch is calculated as $F_{xx} = 1 + \dot{\varepsilon}_{xx}^0 t$, with $\dot{\varepsilon}_{xx}^0$ being the initial strain rate in the axial direction and t the loading time. Recall from Section 3.1 the relationship between the initial strain rate in the axial direction $\dot{\varepsilon}_{xx}^0$ and the imposed initial equivalent strain rate $\dot{\bar{\varepsilon}}^0$, see equation (25). On the other hand, the equivalent strain is measured in the thickest section of the specimen, in the finite element located at the upper right corner of the cell, as indicated in Fig. 3 (see also refs. [39] and [35]). For both cell lengths investigated, $L^0/h^0 = 1$ in Fig. 4(a) and $L^0/h^0 = 3.5$ in Fig. 4(b), the equivalent strain first increases almost linearly with the axial stretch and then saturates to a maximum. The saturation indicates that the ends of the cell are unloading, and that the plastic strain has localized in the center of the specimen giving rise to a necking instability (see ref. [35]). Hence, we will refer to the maximum value of the equivalent strain as necking strain $\bar{\varepsilon}^{neck}$. Similarly, the axial stretch for which the saturation of the equivalent strain occurs will be referred to as necking stretch F_{xx}^{neck} (the same notation we used in Section 5.1). Namely, in the finite element calculations we assume that F_{xx}^{neck} is the axial stretch for which the condition ${}^{d\bar{\varepsilon}}/_{dF_{xx}} = 10^{-3}$ is met. Note that the necking stretch under quasi-static loading is hardly dependent on the material considered (see Table 2 in Section 5.1). In contrast, the necking strain increases as the ratio between the yield stresses in uniaxial tension and pure shear, σ_T/τ_Y, decreases (see Table 2 in Section 5.1). The influence of the value of c on the necking strain arises from the differences in the equivalent strain rate for the 4 materials investigated, see equation (21) in Section 2.3. As the ratio σ_T/τ_Y decreases, i.e. as the parameter c decreases, the rate of accumulation of plastic deformation is greater, which rises the slope of the increasing portion of the $\bar{\varepsilon} - F_{xx}$ curves. Since the necking stretch is approximately the same for the 4 materials for this low strain rate (as mentioned before), the greater the slope of the increasing portion of the $\bar{\varepsilon} - F_{xx}$ curves, the greater the necking strain. Note that the difference in the necking strain obtained for $c = -1.5$ and $c = 2.25$ is approximately 10% for both cell lengths investigated, see also Table 2 in Section 5.1. Moreover, the comparison between the results for $L^0/h^0 = 1$, Fig. 4(a), and $L^0/h^0 = 3.5$, Fig. 4(b), shows that the necking strain and the necking stretch are significantly greater for the smaller cell size, for the 4 materials considered. The larger values of $\bar{\varepsilon}^{neck}$ and F_{xx}^{neck} obtained for $L^0/h^0 = 1$ are caused by the stabilizing effect of stress multiaxiality on short cell sizes, see refs. [39] and [35].

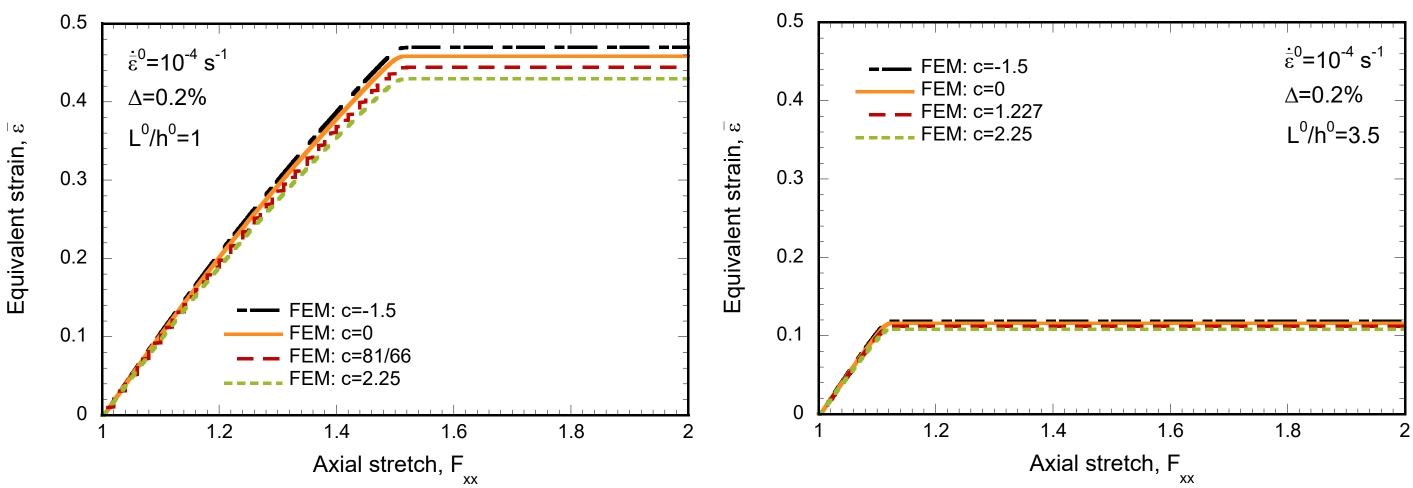

(a) (b)

Figure 4: Finite element results obtained with Drucker yield criterion [11] for Material 1 (von Mises material, $c = 0$ and $\sigma_T/\tau_Y = \sqrt{3}$), Material 2 ($c = -1.5$ and $\sigma_T/\tau_Y = 1.674$), Material 3 (Hershey-Hosford for a BCC material, $c = 81/66$ and $\sigma_T/\tau_Y = 1.790$) and Material 4 ($c = 2.25$ and $\sigma_T/\tau_Y = 1.852$). The initial equivalent strain rate is $\dot{\bar{\varepsilon}}^0 = 10^{-4}$ s^{-1}. Inertia effects are not considered in the finite element simulations. The amplitude of the imperfection is $\Delta = 0.2\%$. Equivalent strain $\bar{\varepsilon}$ versus axial stretch F_{xx}. (a) $L^0/h^0 = 1$ and (b) $L^0/h^0 = 3.5$

Fig. 5 shows the necking strain $\bar{\varepsilon}^{neck}$ and the necking stretch F_{xx}^{neck} versus the cell size L^0/h^0. The necking strain and the necking stretch decrease with the cell size so that the $\bar{\varepsilon}^{neck} - L^0/h^0$ and $F_{xx}^{neck} - L^0/h^0$ curves display a concave-upward shape for the 4 materials considered. The decrease rate of $\bar{\varepsilon}^{neck}$ and F_{xx}^{neck} slows down as L^0/h^0 increases so that for long cell sizes the necking strain and the necking stretch are practically constant. Similar finite element results were reported by Xue et al. [50] who showed that, under quasi-static loading, long wavelength imperfections are the most deleterious, and the necking strain shows little dependence on the wavelength if $L^0/h^0 > 3$. As mentioned before, the increasing necking strains obtained as the cell size decreases are caused by the stabilizing effects of stress multiaxiality on short wavelengths. Moreover, note that the necking strain is greater as c decreases for all the wavelengths, i.e. the trend noted in Fig. 4 for $L^0/h^0 = 1$ and $L^0/h^0 = 3.5$ is the same for the whole range of cell sizes investigated. Similarly, the necking stretch is practically independent of the material for all wavelengths. Note that for $L^0/h^0 = 6$, the necking strain and the necking stretch calculated using finite elements for the 4 materials investigated are very close to the theoretical predictions obtained using the Considère criterion [10], see Table 2. In other words, for long wavelengths and quasi-static loading, the effect of the imperfection on the necking strain and the necking stretch is very small.

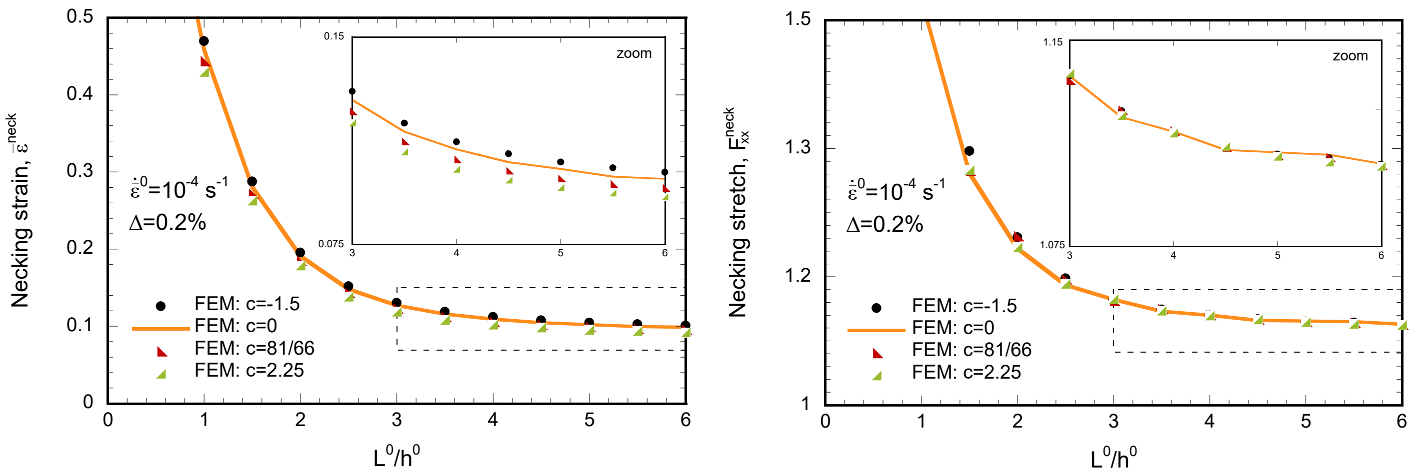

(a) (b)

Figure 5: Finite element results obtained with Drucker yield criterion [11] for Material 1 (von Mises material, $c = 0$ and $\sigma_T/\tau_Y = \sqrt{3}$), Material 2 ($c = -1.5$ and $\sigma_T/\tau_Y = 1.674$), Material 3 (Hershey-Hosford for a BCC material, $c = 81/66$ and $\sigma_T/\tau_Y = 1.790$) and Material 4 ($c = 2.25$ and $\sigma_T/\tau_Y = 1.852$). The initial equivalent strain rate is $\dot{\bar{\varepsilon}}^0 = 10^{-4}$ s^{-1}. Inertia effects are not considered in the finite element simulations. (a) Necking strain $\bar{\varepsilon}^{neck}$ versus L^0/h^0. (b) Necking stretch F_{xx}^{neck} versus L^0/h^0. The amplitude of the imperfection is $\Delta = 0.2\%$.

6. Effect of the third invariant on the formation of dynamic necks in materials with the same response in tension and compression and yielding according to Drucker criterion [11]

In this section, we investigate the influence of inertia on the necking strain and the necking stretch for dynamic conditions. For that purpose, finite element calculations are performed for initial equivalent strain rates ranging from 400 s^{-1} to 80000 s^{-1}, for the four materials obeying Drucker yield criterion [11]. Note that the largest strain rates investigated exceed the regular experimental capabilities. For instance, the dynamic expansion of thin-walled cylinders and hemispherical shells, which is frequently used to investigate the formation of dynamic necks, can rarely be performed for strain rates higher than 20000 s^{-1}, see refs. [53] and [30]. However, exploring loading rates greater than 20000 s^{-1} helps to bring out and understand the effect of the third invariant of the stress deviator on the inception of dynamic necks under plane strain tension. For the given range of initial equivalent strain rates, the parameter describing the inertial resistance to motion $\tilde{L}^{-1}$ varies between 0.00166 and 0.333 (see equation (31)). Note that previous numerical results reported by N'souglo et al. [36, 35] and Zheng et al. [54] indicated that dynamic effects start to play an important role in the inception of necks for $\tilde{L}^{-1}$ in the range $0.06 - 0.1$. The finite element results are compared with the predictions of the linear stability analysis.

6.1. Calibration of the linear stability analysis

The comparison between finite elements and linear stability analysis requires to define a criterion for the perturbation mode to turn into a necking mode. For that purpose, Dudzinski and Molinari [12] introduced the concept of *effective instability*, which is based on the assumption that a neck is triggered when the instability index reaches a critical value. This critical value is known as the *critical instantaneous instability index* $\hat{\eta}_c^+$ or the *critical cumulative instability index* I_c, depending on whether it refers to the instantaneous instability index or to the cumulative instability index (see Section 3.2).

Based on a previous work of Vaz-Romero et al. [47], N'souglo et al. [35] has recently developed a methodology to determine I_c with finite element simulations. Using the unit-cell model presented in Fig. 3, N'souglo et al. [35] obtained, for a von Mises material ($c = 0$) described with the parameters given in Table 1, the evolution of the necking strain $\bar{\varepsilon}^{neck}$ with the cell size L^0/h^0 reported in Fig. 6 (black solid markers). The calculations were performed in ABAQUS/Explicit, accounting for inertia effects. The amplitude of the imperfection was $\Delta = 0.2\%$ (as in the finite element calculations presented in this work), and the imposed initial equivalent strain rate was $\dot{\bar{\varepsilon}}^0 = 40000$ s^{-1}. Note that, unlike the quasi-static loading results reported in Fig. 5(a), the $\bar{\varepsilon}^{neck} - L^0/h^0$ curve for $\dot{\bar{\varepsilon}}^0 = 40000$ s^{-1} shows a minimum for an intermediate cell size, with the corresponding strain being referred to as the critical necking strain $\bar{\varepsilon}_c^{neck}$, see Fig. 16(b). The minimum is the result of the stabilizing effect of stress multiaxiality and inertia on short and long cell sizes, respectively (we will further elaborate on this issue in Section 6.3). The value of the minimum necking strain is 0.475, and the corresponding cell size, referred to as the critical cell size in Rodríguez-Martínez et al. [40, 39], is $\left(L^0/h^0\right)_c^{FEM} \approx 2.2$. Using this minimum of the necking strain as the equivalent strain for which the cumulative index is calculated, the maximum value of I, which corresponds to the critical cumulative perturbation wavelength, is 3.75, see Fig. 7. N'souglo et al. [35] took this value of I as the cumulative instability index required to trigger a neck, i.e. as the critical cumulative instability index $I_c = 3.75$. Following an analogous procedure for the instantaneous index, in this work we have also obtained the critical instantaneous instability index $\hat{\eta}_c^+ = 19$ (see Fig. 7). Note that for the determination of $\hat{\eta}_c^+$ and I_c we use as input data only the necking strain corresponding to the critical cell size obtained from the finite element calculations (i.e. the critical necking strain $\bar{\varepsilon}_c^{neck}$, see Fig. 16(b)). Predictions of the linear stability analysis for wavelengths other than the critical are presented in Section 6.2.

6.2. Comparison between critical instantaneous instability index and critical cumulative instability index

Fig. 6 shows a comparison for a von Mises material ($c = 0$) between the equivalent strains calculated with the stability analysis using the criteria $I = I_c$ (green line) and $\hat{\eta}^+ = \hat{\eta}_c^+$ (red line), and the necking strains calculated with the finite element simulations for a wide range of wavelengths L^0/h^0. The equivalent strains corresponding to the criteria $I = I_c$ and $\hat{\eta}^+ = \hat{\eta}_c^+$ are the counterpart of the necking strains $\bar{\varepsilon}^{neck}$ in the finite element calculations and thus will be denoted the same way. The perturbation analysis results obtained with both criteria show qualitative agreement with the finite element calculations: the value of $\bar{\varepsilon}^{neck}$ first decreases with L^0/h^0, reaches a minimum $\bar{\varepsilon}_c^{neck}$, and then increases. However, the predictions obtained with the critical cumulative instability index I_c find better quantitative agreement with the finite element results. For example, the critical cumulative perturbation wavelength $\left(L^0/h^0\right)_c^{I} \approx 2.1$, which corresponds to the minimum of the $\bar{\varepsilon}^{neck} - \left(L^0/h^0\right)$ curve obtained for $I_c = 3.75$, is very similar to the critical cell size $\left(L^0/h^0\right)_c^{FEM} \approx 2.2$ obtained in the finite element calculations. In contrast, the critical instantaneous perturbation wavelength is significantly smaller $\left(L^0/h^0\right)_c^{\hat{\eta}^+} \approx 1.3$. Note that the differences between the predictions obtained with the critical instantaneous instability index $\hat{\eta}_c^+ = 19$ and the finite element results are particularly important for long wavelengths. For $\left(L^0/h^0\right) > \left(L^0/h^0\right)_c^{\hat{\eta}^+}$, the criterion $\hat{\eta}_c^+ = 19$ predicts a severe increase of $\bar{\varepsilon}^{neck}$ which is not shown by the finite element results.

A key outcome of this paper is to demonstrate that at high strain rates the critical cumulative instability index I_c provides predictions closer to the finite element results than the critical instantaneous instability index $\hat{\eta}_c^+$. Note that additional comparisons between finite element results and stability analysis predictions which support this statement are presented in Appendix B for a von Mises material ($c = 0$) and five different imposed equivalent strain rates: 400 s^{-1}, 4000 s^{-1}, 10000 s^{-1}, 20000 s^{-1} and 80000 s^{-1}. Hence, most of the stability analysis results presented in Section 6.3 are obtained with $I_c = 3.75$ (we only show selected results with $\hat{\eta}_c^+ = 19$). As N'souglo et al. [35], we assume that this critical value of the cumulative instability index is the same for all the initial equivalent strain rates and materials investigated in this work. We are aware that this is a rather crude assumption, however, considering $I_c = constant$ facilitates the comparison between stability analysis predictions and finite element simulations, and the interpretation of results, while providing trends for the necking strain and the necking stretch that are in qualitative agreement with the unit-cell calculations. Nevertheless, for the sake of completeness, in Appendix C we show stability analysis predictions obtained for a von Mises material ($c = 0$) with a critical cumulative index which depends nonlinearly on the strain rate. The comparison with finite element calculations shows that accounting for the strain rate dependence of I_c improves the predictions of the stability analysis, yet at the expense of needing additional calibration data.

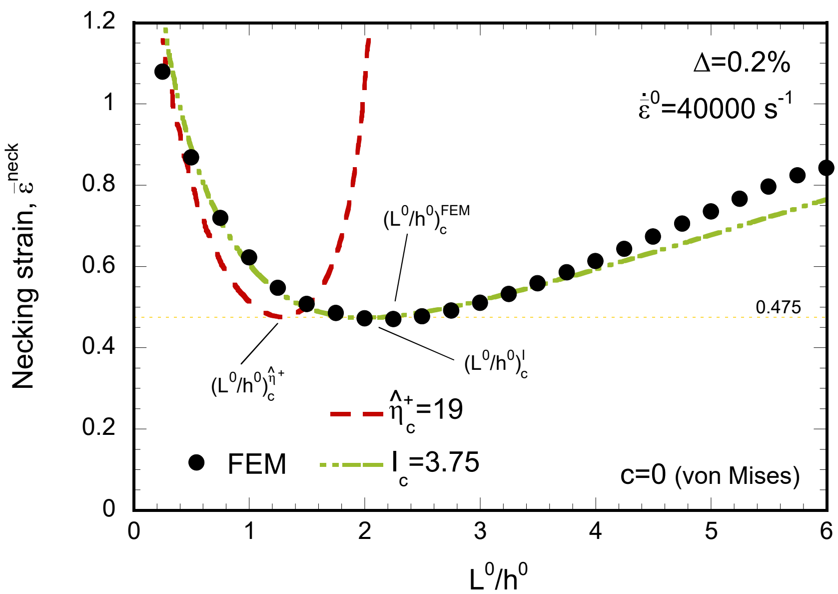

Figure 6: Comparison between finite element results (FEM) and linear stability analysis predictions (LSA) for Material 1 (von Mises material, $c = 0$ and $\sigma_T/\tau_Y = \sqrt{3}$). Necking strain $\bar{\varepsilon}^{neck}$ obtained using finite element simulations (FEM) and linear stability analysis (LSA) versus L^0/h^0. Linear stability analysis results are shown for both criteria $I_c = 3.75$ and $\hat{\eta}_c^+ = 19$. In the finite element simulations the amplitude of the imperfection is $\Delta = 0.2\%$. The initial equivalent strain rate is $\dot{\bar{\varepsilon}}^0 = 40000\ \mathrm{s}^{-1}$. (For interpretation of the references to color in the text, the reader is referred to the web version of this article.)

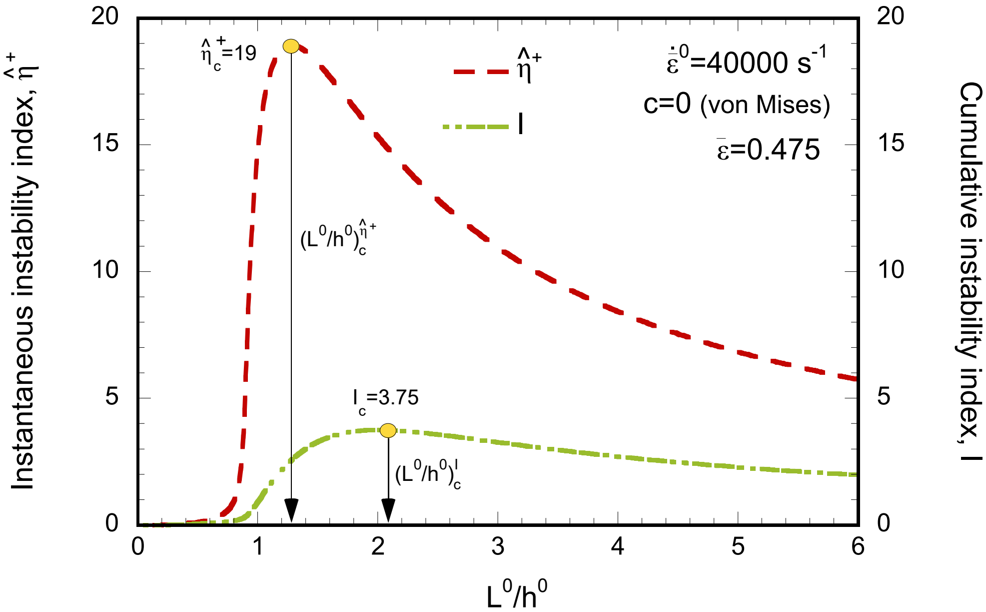

Figure 7: Stability analysis results. Instantaneous instability index $\hat{\eta}^+$ and cumulative instability index I versus perturbation wavelength L^0/h^0 for Material 1 (von Mises material, $c = 0$ and $\sigma_T/\tau_Y = \sqrt{3}$). The initial equivalent strain rate is $\dot{\bar{\varepsilon}}^0 = 40000$ s^{-1}. The equivalent strain is $\bar{\varepsilon} = 0.475$. The figure indicates the critical instantaneous instability index $\hat{\eta}_c^+ = 19$, the critical cumulative instability index $I_c = 3.75$, and the corresponding critical perturbation wavelengths $\left(L^0/h^0\right)_c^{\hat{\eta}^+} \approx 1.3$ and $\left(L^0/h^0\right)_c^{I} \approx 2.1$.

6.3. Comparison between finite element results and stability analysis predictions for materials obeying Drucker criterion [11]

Fig. 8 shows finite element results for the evolution of the equivalent strain $\bar{\varepsilon}$ with the axial stretch F_{xx} for two different normalized cell lengths, $L^0/h^0 = 0.5$ and $L^0/h^0 = 3.5$. Recall from Section 5.2 that the equivalent strain $\bar{\varepsilon}$ is measured in the thickest section of the specimen, in the finite element located at the upper right corner of the cell (see Fig. 3), and the axial stretch is calculated as $F_{xx} = 1 + \dot{\varepsilon}_{xx}^0\, t$. The results correspond to Material 2 ($c = -1.5$ and $\sigma_T/\tau_Y = 1.674$), Material 3 (Hershey-Hosford for a BCC material, $c = 81/66$ and $\sigma_T/\tau_Y = 1.790$) and Material 4 ($c = 2.25$ and $\sigma_T/\tau_Y = 1.852$). In this section, we do not show results for the von Mises material (Material 1, $c = 0$ and $\sigma_T/\tau_Y = \sqrt{3}$). As mentioned, the normalized imperfection amplitude in all the finite element simulations presented in this paper is $\Delta = 0.2\%$. The initial equivalent strain rate is $\dot{\bar{\varepsilon}}^0 = 400$ s^{-1}. The value of the inertia parameter is $\tilde{L}^{-1} = 0.00166$. We have also included the finite element results corresponding to the quasi-static case for $L^0/h^0 = 3.5$ and $c = 81/66$, which show that, for this strain rate, inertia has a minor contribution on the response of the cell since the $\bar{\varepsilon} - F_{xx}$ curves for quasi-static loading and 400 s^{-1} virtually overlap each other.

The equivalent strain first increases with the axial stretch and then saturates to a maximum which corresponds to the necking strain $\bar{\varepsilon}^{neck}$ (see Section 5.2). For both cell sizes, $L^0/h^0 = 0.5$ and $L^0/h^0 = 3.5$, the necking strain is greater as the ratio σ_T/τ_Y decreases, i.e. as the parameter c decreases. On the other hand, the axial stretch for which the necking strain is reached, i.e. the necking stretch F_{xx}^{neck}, is *hardly* dependent on c. Similar results were reported in Fig. 4 for an imposed initial equivalent strain rate of 10^{-4} s^{-1}.

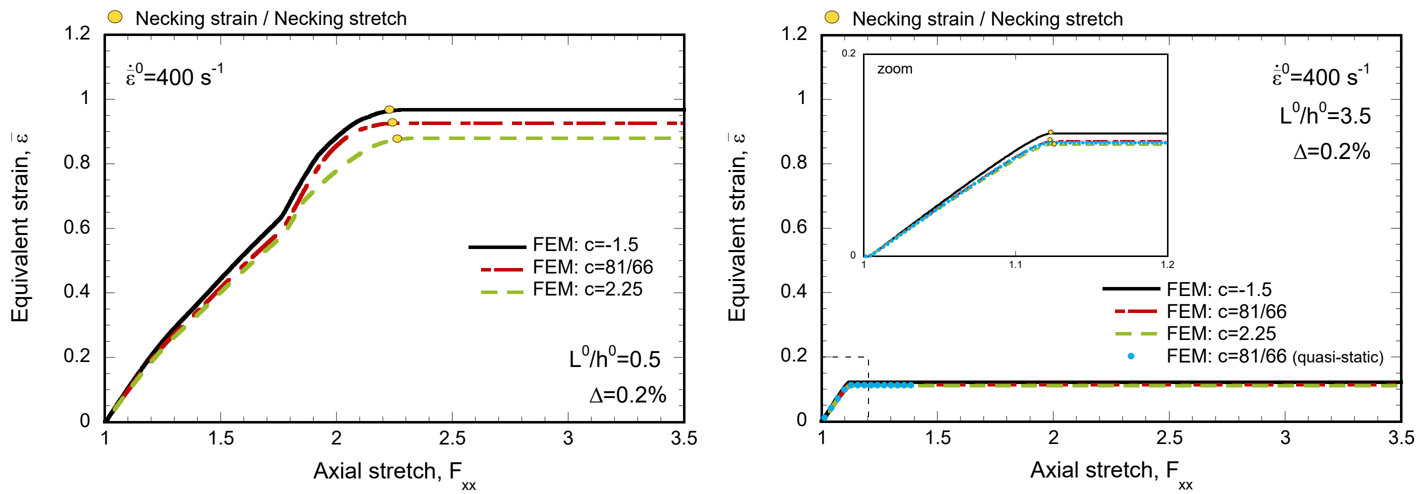

(a) (b)

Figure 8: Finite element results obtained with Drucker yield criterion [11] for Material 2 ($c = -1.5$ and $\sigma_T/\tau_Y = 1.674$), Material 3 (Hershey-Hosford for a BCC material, $c = 81/66$ and $\sigma_T/\tau_Y = 1.790$) and Material 4 ($c = 2.25$ and $\sigma_T/\tau_Y = 1.852$), respectively. The initial equivalent strain rate is $\dot{\bar{\varepsilon}}^0 = 400$ s^{-1}. The amplitude of the imperfection is $\Delta = 0.2\%$. Equivalent strain $\bar{\varepsilon}$ versus axial stretch F_{xx}. (a) $L^0/h^0 = 0.5$ and (b) $L^0/h^0 = 3.5$. We have also included the finite element results corresponding to the quasi-static case for $L^0/h^0 = 3.5$ and $c = 81/66$.

Fig. 9 presents a comparison between finite element results and linear stability analysis predictions for the same materials ($c = -1.5$, 81/66 and 2.25) and the same initial equivalent strain rate (400 s^{-1}) considered in Fig. 8. The stability analysis predictions are obtained with the criterion $I_c = 3.75$ (like the vast majority of the analytical results presented in this section). Note that for $c = 81/66$ we also include stability analysis results obtained with the critical instantaneous instability index $\hat{\eta}_c^+ = 19$.

Fig. 9(a) displays the evolution of the necking strain $\bar{\varepsilon}^{neck}$ with L^0/h^0. The $\bar{\varepsilon}^{neck} - L^0/h^0$ finite element curves display a concave-upward shape such that the decrease of the necking strain slows down as the wavelength increases. The monotonic decrease of $\bar{\varepsilon}^{neck}$ occurs because, for this imposed initial strain rate, inertia effects are small (see the quasi-static results in Fig. 5). The value of $\bar{\varepsilon}^{neck}$ is slightly greater as the ratio σ_T/τ_Y decreases, i.e. as the parameter c decreases. Note that the predictions of the linear stability analysis obtained with the critical cumulative index show qualitative and quantitative agreement with the finite element calculations for the three materials considered. In addition, the results obtained with $\hat{\eta}_c^+ = 19$ for $c = 81/66$ are very similar to the predictions obtained with $I_c = 3.75$, and slightly closer to the finite element results for the longer wavelengths investigated.

Fig. 9(b) shows the evolution of the necking stretch F_{xx}^{neck} with L^0/h^0. In the linear stability analysis the necking stretch is computed as $F_{xx}^{neck} = e^{\frac{A^{1/6}}{2}\bar{\varepsilon}^{neck}}$, see equation (34). Note that the necking stretch calculated using both finite elements and stability analysis with $I_c = 3.75$ decreases nonlinearly with the wavelength, like the necking strain in Fig. 9(a). The influence of the ratio σ_T/τ_Y is negligible for all the wavelengths investigated. As in Fig. 9(a), the stability analysis predictions obtained with $I_c = 3.75$ show very good qualitative and quantitative agreement with the finite element results for the whole range of wavelengths investigated. Note that the results obtained with $\hat{\eta}_c^+ = 19$ for $c = 81/66$ are also very close to the finite element calculations.

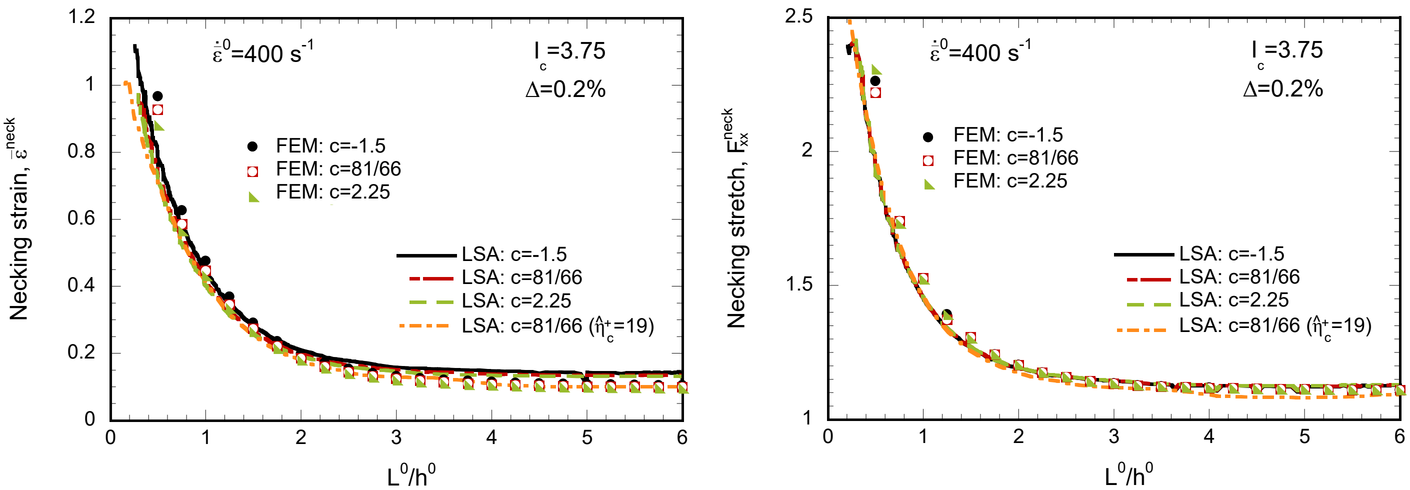

(a) (b)

Figure 9: Comparison between finite element results (FEM) and linear stability analysis predictions (LSA) obtained with Drucker yield criterion [11] for Material 2 ($c = -1.5$ and $\sigma_T/\tau_Y = 1.674$), Material 3 (Hershey-Hosford for a BCC material, $c = 81/66$ and $\sigma_T/\tau_Y = 1.790$) and Material 4 ($c = 2.25$ and $\sigma_T/\tau_Y = 1.852$), respectively. The initial equivalent strain rate is $\dot{\bar{\varepsilon}}^0 = 400\ \mathrm{s}^{-1}$. (a) Necking strain $\bar{\varepsilon}^{neck}$ versus L^0/h^0. (b) Necking stretch F_{xx}^{neck} versus L^0/h^0. In the finite element simulations the amplitude of the imperfection is $\Delta = 0.2\%$. In the linear stability analysis the critical cumulative instability index is $I_c = 3.75$. For $c = 81/66$ we also include stability analysis results obtained with the critical instantaneous instability index $\hat{\eta}_c^+ = 19$.

Fig. 10 presents a comparison between finite element results and linear stability analysis predictions obtained with $I_c = 3.75$ for the same materials ($c = -1.5$, $81/66$ and 2.25) considered in Fig. 9, and greater initial equivalent strain rate ($4000\ \mathrm{s}^{-1}$). The value of the inertia parameter is $\tilde{L}^{-1} = 0.0166$. We have also included stability analysis results obtained with the critical instantaneous instability index $\hat{\eta}_c^+ = 19$ for $c = 81/66$.

Fig. 10(a) displays the evolution of the necking strain $\bar{\varepsilon}^{neck}$ with L^0/h^0. Unlike the results presented in Figs. 5(a) and 9(a) for lower strain rates, the $\bar{\varepsilon}^{neck} - L^0/h^0$ curves for $4000\ \mathrm{s}^{-1}$ show a *(shallow)* minimum due to the incipient stabilizing role of inertia effects. In the case of the finite element calculations the minimum corresponds to the critical cell size $(L^0/h^0)_c^{FEM} \approx 4.25$, and in the case of the linear stability analysis results obtained with

$I_c = 3.75$, to the critical cumulative perturbation wavelength $\left(L^0/h^0\right)_c^I \approx 3.64$. In comparison with the results obtained for lower strain rates, the necking strain $\bar{\varepsilon}^{neck}$ is slightly greater, particularly, for long wavelengths (nevertheless, the differences are hardly noticeable unless the curves for different loading rates are superimposed). Moreover, similarly to the results presented in Figs. 5(a) and 9(a), the value of $\bar{\varepsilon}^{neck}$ slightly increases as c decreases. Note that there is qualitative agreement between stability analysis predictions with $I_c = 3.75$ and finite element results. However, quantitative differences appear for the longest wavelengths investigated, for which the necking strains calculated with the finite elements are $\approx 50\%$ smaller than the predictions of the linear stability analysis. In fact, for long wavelengths, the results obtained with $\hat{\eta}_c^+ = 19$ find better agreement with the finite element calculations.

Fig. 10(b) shows the evolution of the necking stretch F_{xx}^{neck} with L^0/h^0. The theoretical predictions with $I_c = 3.75$ are very close to the finite element results for the whole range of wavelengths investigated. Moreover, similarly to the results presented in Figs. 5(b) and 9(b), the necking stretch F_{xx}^{neck} is largely independent of the value of c, which accounts for the ratio between the yield stresses in uniaxial tension and pure shear. Moreover, for long wavelengths, the stability analysis predictions obtained with the instantaneous instability index $\hat{\eta}_c^+ = 19$ underestimate the finite element results.

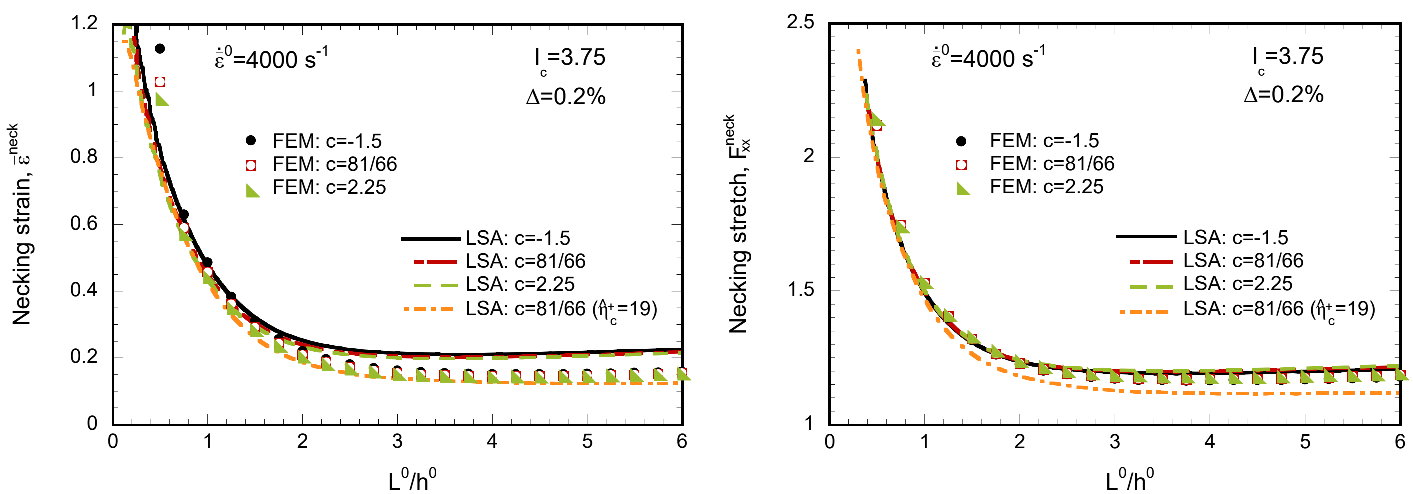

(a) (b)

Figure 10: Comparison between finite element results (FEM) and linear stability analysis predictions (LSA) obtained with Drucker yield criterion [11] for Material 2 ($c = -1.5$ and $\sigma_T/\tau_Y = 1.674$), Material 3 (Hershey-Hosford for a BCC material, $c = 81/66$ and $\sigma_T/\tau_Y = 1.790$) and Material 4 ($c = 2.25$ and $\sigma_T/\tau_Y = 1.852$), respectively. The initial equivalent strain rate is $\dot{\bar{\varepsilon}}^0 = 4000$ s^{-1}. (a) Necking strain $\bar{\varepsilon}^{neck}$ versus L^0/h^0. (b) Necking stretch F_{xx}^{neck} versus L^0/h^0. In the finite element simulations the amplitude of the imperfection is $\Delta = 0.2\%$. In the linear stability analysis the critical cumulative instability index is $I_c = 3.75$. For $c = 81/66$ we also include stability analysis results obtained with the critical instantaneous instability index $\hat{\eta}_c^+ = 19$.

Fig. 11 shows finite element results and linear stability analysis predictions obtained with $I_c = 3.75$ for greater initial equivalent strain rate $\dot{\bar{\varepsilon}}^0 = 40000$ s^{-1}. The value of the inertia parameter is $\tilde{L}^{-1} = 0.166$. Stability analysis results obtained with the critical instantaneous instability index $\hat{\eta}_c^+ = 19$ for $c = 81/66$ are also included.

Fig. 11(a) displays the evolution of the necking strain $\bar{\varepsilon}^{neck}$ with L^0/h^0. The stability analysis predictions with $I_c = 3.75$ are in qualitative and quantitative agreement with the finite element simulations. The necking strain $\bar{\varepsilon}^{neck}$ displays a minimum for an intermediate cell length, so that the critical cell size and the critical cumulative perturbation wavelength are $\left(L^0/h^0\right)_c^{FEM} \approx 2.2$ and $\left(L^0/h^0\right)_c^{I} \approx 2.1$, respectively (these values are hardly dependent on the ratio σ_T/τ_Y, see also Section 6.2 and Fig. 16(a)). Moreover, note that, unlike what happens for lower initial equivalent strain rates, see Figs. 5(a), 9(a) and 10(a), the effect of the value of c on the necking strain depends on the wavelength. The $\bar{\varepsilon}^{neck} - L^0/h^0$ curves obtained for the three materials considered intersect for an intermediate wavelength so that Material 2 ($c = -1.5$) displays the greatest necking strain for short wavelengths, and the smallest necking strain for long wavelengths (nevertheless, the differences in the necking strains for the three materials are small). These results also reveal that the specific influence of the value of c on the necking strain depends on the imposed initial equivalent strain rate, i.e. on inertia effects. On the other hand, notice that the stability analysis with $\hat{\eta}_c^+ = 19$ predicts a drastic increase in the necking strain which is not consistent with the finite element results (see also Fig. 7 and Appendix B.)

Fig. 11(b) shows the necking stretch F_{xx}^{neck} versus the wavelength L^0/h^0. Both stability analysis predictions with $I_c = 3.75$ and finite element results show that the influence of the value of c on the necking stretch increases with the wavelength. The greatest values of F_{xx}^{neck} correspond to Material 4 ($c = 2.25$), and the smallest to Material 2 ($c = -1.5$). These results stand in contrast with those obtained for lower strain rates, see Figs. 5(b), 9(b) and 10(b), for which the influence of the value of c on the necking stretch was negligible. The difference is that, for $\dot{\bar{\varepsilon}}^0 = 40000$ s^{-1}, inertia effects have become important, especially for long wavelengths. The greater the strain rate in the loading direction (see equation (25)), the greater the extent of the post-critical deformation regime, and thus the necking stretch. The initial strain rate in the axial direction $\dot{\varepsilon}_{xx}^0$ for Materials 2, 3 and 4 is 33501.6 s^{-1}, 35818.9 s^{-1} and 37061.5 s^{-1}, respectively. These results show that the loading rate scales the influence of the value of c on the necking stretch. On the other hand, despite the good qualitative agreement between stability analysis predictions with $I_c = 3.75$ and finite element results, the quantitative differences between both approaches are above 25% for long wavelengths (note that the difference is even greater for the stability analysis predictions obtained with the instantaneous instability index $\hat{\eta}_c^+ = 19$). A probable reason for the disagreement is that I_c is taken to be constant. In this regard, it is reasonable to argue that the critical cumulative index is strain rate dependent, so that as the strain rate increases the value of I_c shall also increase to account for the stabilization of the material with increasing inertia effects. In Appendix C we show additional stability analysis results for a von Mises material ($c = 0$) in which the critical cumulative index is strain rate dependent. As mentioned before, the comparison with the unit cell finite element calculations shows that accounting for the strain rate dependence of I_c improves the predictions of the stability analysis, yet at the expense of needing additional calibration data.

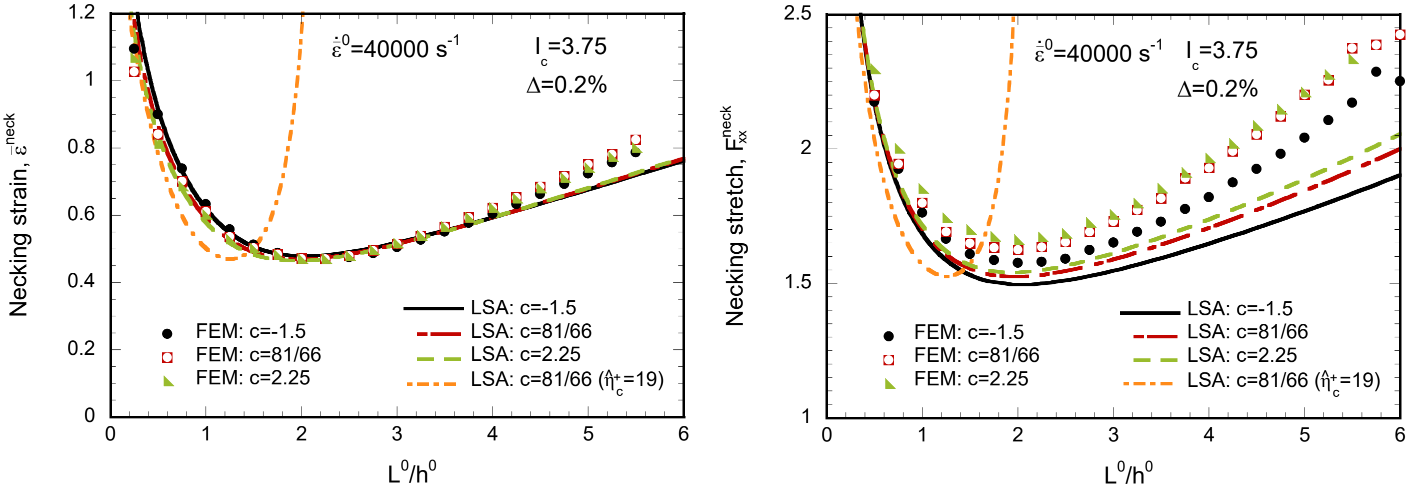

(a) (b)

Figure 11: Comparison between finite element results (FEM) and linear stability analysis predictions (LSA) obtained with Drucker yield criterion [11] for Material 2 ($c = -1.5$ and $\sigma_T/\tau_Y = 1.674$), Material 3 (Hershey-Hosford for a BCC material, $c = 81/66$ and $\sigma_T/\tau_Y = 1.790$) and Material 4 ($c = 2.25$ and $\sigma_T/\tau_Y = 1.852$), respectively. The initial equivalent strain rate is $\dot{\bar{\varepsilon}}^0 = 40000$ s^{-1}. (a) Necking strain $\bar{\varepsilon}^{neck}$ versus L^0/h^0. (b) Necking stretch F^{neck}_{xx} versus L^0/h^0. In the finite element simulations the amplitude of the imperfection is $\Delta = 0.2\%$. In the linear stability analysis the critical cumulative instability index is $I_c = 3.75$. For $c = 81/66$ we also include stability analysis results obtained with the critical instantaneous instability index $\hat{\eta}^+_c = 19$.

Moreover, Fig. 12 displays contours of equivalent strain $\bar{\varepsilon}$ obtained with Drucker yield criterion [11] for Material 2 ($c = -1.5$ and $\sigma_T/\tau_Y = 1.674$) corresponding to the necking condition, and for two different values of the initial equivalent strain rate, $\dot{\varepsilon}^0 = 10^{-4}$ s^{-1} and 40000 s^{-1}. The amplitude of the imperfection is $\Delta = 0.2\%$ and $L^0/h^0 = 3.5$. Note that for the higher strain rate, the relative variation of the equivalent strain is less pronounced than in the quasi-static case.

Fig. 13 presents finite element results and linear stability analysis predictions with $I_c = 3.75$ for the greatest initial equivalent strain rate investigated in this work, $\dot{\bar{\varepsilon}}^0 = 80000$ s^{-1}, for which the value of the inertia parameter is $\tilde{L}^{-1} = 0.333$. We also show the stability analysis predictions obtained with the critical instability index $\hat{\eta}^+_c = 19$ for $c = 81/66$.

Fig. 13(a) shows the evolution of the necking strain $\bar{\varepsilon}^{neck}$ with L^0/h^0. The linear stability analysis predictions with $I_c = 3.75$ are in qualitative agreement with the finite element results. The $\bar{\varepsilon}^{neck} - L^0/h^0$ curves obtained for the three different materials intersect for an intermediate wavelength. As in the case of $\dot{\bar{\varepsilon}}^0 = 40000$ s^{-1} reported

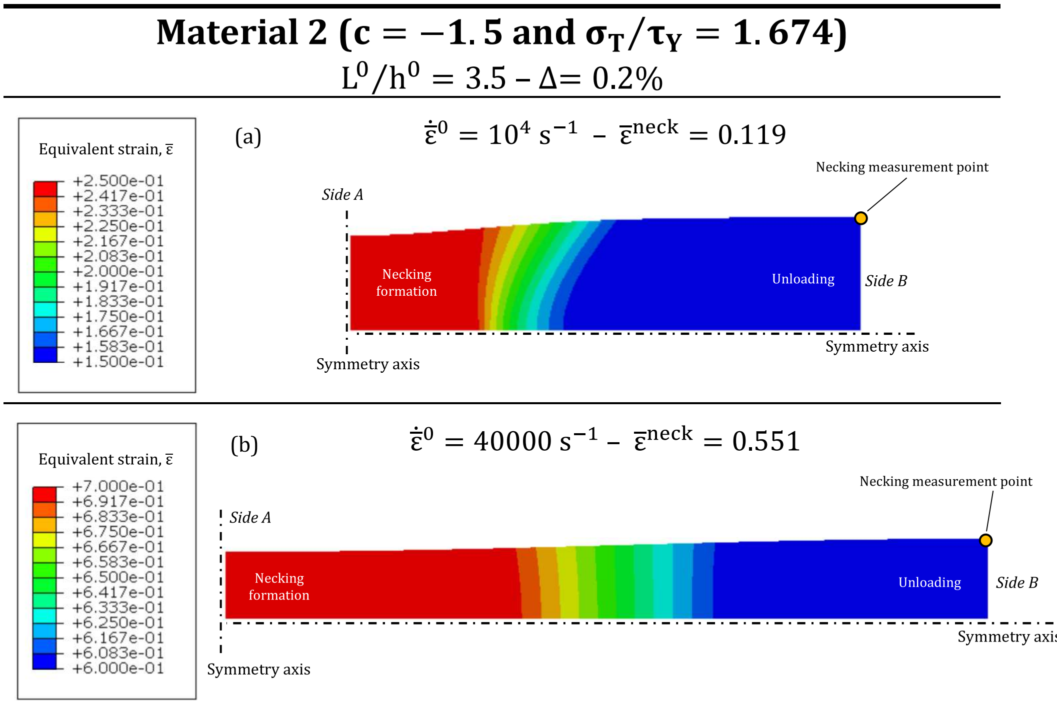

Figure 12: Contours of equivalent strain $\bar{\varepsilon}$ obtained with Drucker yield criterion [11] for Material 2 ($c = -1.5$ and $\sigma_T/\tau_Y = 1.674$) corresponding to the necking condition. The amplitude of the imperfection is $\Delta = 0.2\%$ and $L^0/h^0 = 3.5$. Results correspond to: (a) $\dot{\varepsilon}^0 = 10^{-4}$ s^{-1} and $\bar{\varepsilon}^{neck} = 0.119$, (b) $\dot{\varepsilon}^0 = 40000$ s^{-1} and $\bar{\varepsilon}^{neck} = 0.551$.

in Fig. 11(a), Material 2 ($c = -1.5$) shows the greatest necking strain for short values of L^0/h^0, and the smallest for long wavelengths (nevertheless, the differences in the necking strains for the three materials are small). The influence of the ratio σ_T/τ_Y on the necking strain depends on the wavelength (see also Fig. 14). Moreover, the quantitative differences between stability analysis with $I_c = 3.75$ and finite element results, which are negligible for short values of L^0/h^0, increase with the wavelength. For instance, the theoretical predictions underestimate the finite element results by 15% and 23%, for $L^0/h^0 = 2$ and $L^0/h^0 = 4$, respectively. As mentioned before, the quantitative differences between finite element results and stability analysis are partially because the critical cumulative index is taken strain rate independent (see Appendix C for details). Note that N'souglo et al. [34] have already shown that the predictions of the stability model with $I_c = constant$ generally get worse as the strain rate for which the analysis is performed moves away from the strain rate used for the calibration of I_c, especially at higher strain rates, when the role of inertia on material stabilization becomes more important. Moreover, note that the stability analysis predictions obtained with the instantaneous instability index $\hat{\eta}_c^+ = 19$ show a steep increase of the necking strain for long wavelengths that it is not observed in the finite element calculations. In addition, the critical instantaneous perturbation wavelength is significantly smaller $\left(L^0/h^0\right)_c^{\hat{\eta}^+} \approx 0.65$ than in the finite element calculations $\left(L^0/h^0\right)_c^{FEM} \approx 1.7$.

Fig. 13(b) displays the evolution of the necking stretch F_{xx}^{neck} with L^0/h^0. The linear stability analysis with $I_c = 3.75$ predicts smaller values of F_{xx}^{neck} than the finite element results. However, both approaches show the same overall trends. As in the case of $\dot{\bar{\varepsilon}}^0 = 40000$ s^{-1}, the third invariant J_3 has increasing influence on the necking stretch as the wavelength increases. For long wavelengths, F_{xx}^{neck} increases as the relation between the yield stress in uniaxial tension and in pure shear increases, i.e. as the strain rate in the loading direction increases. The differences between $c = -1.5$ and $81/66$ are greater than between $c = 81/66$ and 2.25. Moreover, notice that the theoretical results for $\hat{\eta}_c^+ = 19$ predict values of the necking stretch for $L^0/h^0 > \left(L^0/h^0\right)_c^{\hat{\eta}^+}$ which are much higher than the finite element calculations.

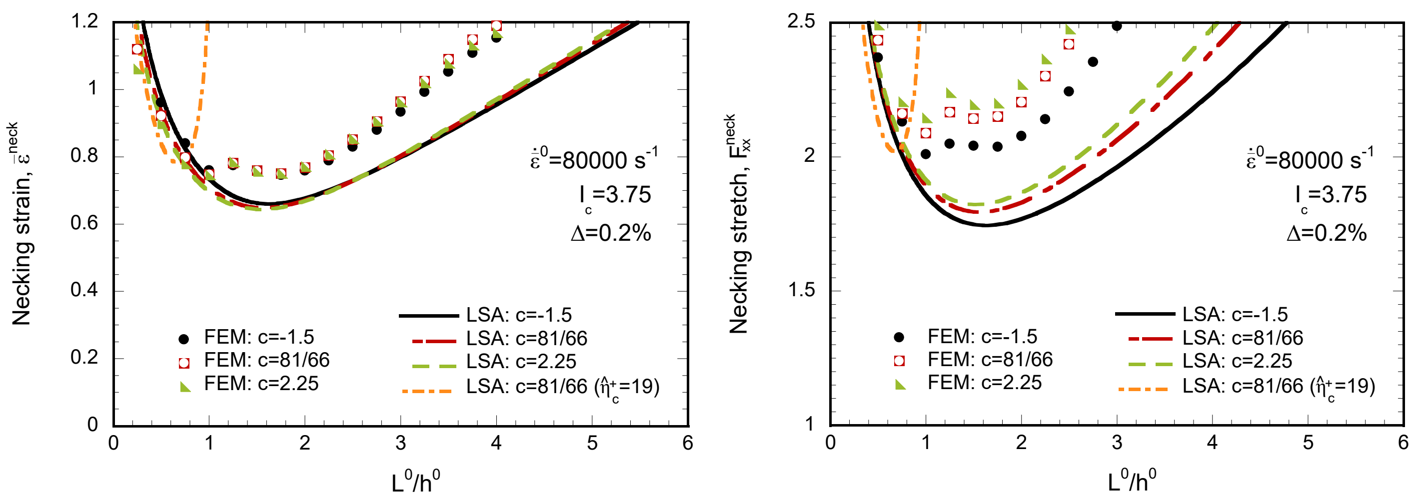

(a) (b)

Figure 13: Comparison between finite element results (FEM) and linear stability analysis predictions (LSA) obtained with Drucker yield criterion [11] for Material 2 ($c = -1.5$ and $\sigma_T/\tau_Y = 1.674$), Material 3 (Hershey-Hosford for a BCC material, $c = 81/66$ and $\sigma_T/\tau_Y = 1.790$) and Material 4 ($c = 2.25$ and $\sigma_T/\tau_Y = 1.852$), respectively. The initial equivalent strain rate is $\dot{\bar{\varepsilon}}^0 = 80000$ s^{-1}. (a) Necking strain $\bar{\varepsilon}^{neck}$ versus L^0/h^0. (b) Necking stretch F_{xx}^{neck} versus L^0/h^0. In the finite element simulations the amplitude of the imperfection is $\Delta = 0.2\%$. In the linear stability analysis the critical cumulative instability index is $I_c = 3.75$. For $c = 81/66$ we also include stability analysis results obtained with the critical instantaneous instability index $\hat{\eta}_c^+ = 19$.

The wavelength-dependent influence of the value of c, which accounts for the ratio σ_T/τ_Y, on $\bar{\varepsilon}^{neck}$ and F_{xx}^{neck} is further illustrated in Fig. 14 which shows finite element results for the evolution of the equivalent strain $\bar{\varepsilon}$ with the axial stretch F_{xx} and two different wavelengths, $L^0/h^0 = 0.5$ and $L^0/h^0 = 3.5$. Recall from Section 5.2 that the axial stretch is calculated as $F_{xx} = 1 + \dot{\varepsilon}_{xx}^0\, t$, and the equivalent strain $\bar{\varepsilon}$ is measured in the finite element located at the upper right corner of the unit-cell (see Fig. 3). As in Fig. 13, the imposed initial equivalent strain rate is 80000 s^{-1}.

Fig. 14(a) shows the finite element results for $L^0/h^0 = 0.5$. The equivalent strain first increases roughly linearly with the axial stretch and then saturates to a maximum. Recall that the maximum value of the equivalent strain is the necking strain $\bar{\varepsilon}^{neck}$, and the stretch corresponding to the saturation of the strain is the necking stretch F_{xx}^{neck}. Since the necking stretch is hardly dependent on the material considered, the necking strain increases as the rate of accumulation of plastic deformation of the material is greater, i.e. as the ratio σ_T/τ_Y decreases (as c decreases). These results bear a close resemblance with those obtained at lower strain rates, for short and long wavelengths, in Figs. 4 and 8.

Fig. 14(b) shows the finite element results for $L^0/h^0 = 3.5$. The necking stretch F_{xx}^{neck} for the material with $c = -1.5$ is $\approx 10\%$ and $\approx 12\%$ smaller than that calculated for the materials with $c = 81/66$ and $c = 2.25$, respectively. Hence, despite of having the greatest rate of accumulation of plastic deformation, the material with $c = -1.5$ shows the smaller necking strain. The comparison of these results with Figs. 4, 8 and 14(a) reveals that for high strain rates and long wavelengths (i.e. for the loading and geometric conditions for which the influence of inertia on the necking process is more important), the minimum necking strain corresponds to the material with the highest rate of accumulation of plastic deformation. As mentioned before, this behavior is attributed to the fact that, for a given value of imposed initial equivalent strain rate $\dot{\bar{\varepsilon}}^0$, the decrease of the value of c leads to a decrease of the initial strain rate in the loading direction $\dot{\varepsilon}_{xx}^0$, which in turn leads to a decrease in the necking stretch, and thus in the necking strain. Note that for $c = -1.5$ the initial strain rate in the loading direction $\dot{\varepsilon}_{xx}^0$ is 67003 s^{-1}, while for $c = 81/66$ and $c = 2.25$ the corresponding values are 71638 s^{-1} and 74123 s^{-1}, respectively. In other words, the wavelength-dependent influence of the third invariant J_3 described through the parameter c on the necking strain is caused by the wavelength-dependent influence of inertia on the necking strain. This is an original result of this investigation that, to the authors' knowledge, has not been reported before.

The effect of inertia on the necking strain as a function of the wavelength is further illustrated in Fig. 15 which shows finite element results for the evolution of the equivalent strain $\bar{\varepsilon}$ with the axial stretch F_{xx}, for three different imposed initial equivalent strain rates: 10^{-4} s^{-1}, 400 s^{-1} and 80000 s^{-1}, and two different wavelengths: $L^0/h^0 = 1$ and $L^0/h^0 = 3.5$. Material 2 ($c = -1.5$) is considered in the calculations.

Fig. 15(a) shows the results for $L^0/h^0 = 1$. The $\bar{\varepsilon} - F_{xx}$ curves for 10^{-4} s^{-1} and 400 s^{-1} are very similar, which shows the negligible influence of inertia effects on necking for this range of strain rates. In contrast, the elongation of the cell when necking occurs doubles from 400 s^{-1} to 80000 s^{-1}, leading to 60% increase in the necking strain, which reveals the stabilizing effect of inertia at high strain rates.

Fig. 15(b) shows the results for $L^0/h^0 = 3.5$. As in the case of $L^0/h^0 = 1$, the $\bar{\varepsilon} - F_{xx}$ curves for 10^{-4} s^{-1} and 400 s^{-1} practically overlap each other. In contrast, the increase of the strain rate up to 80000 s^{-1} leads to

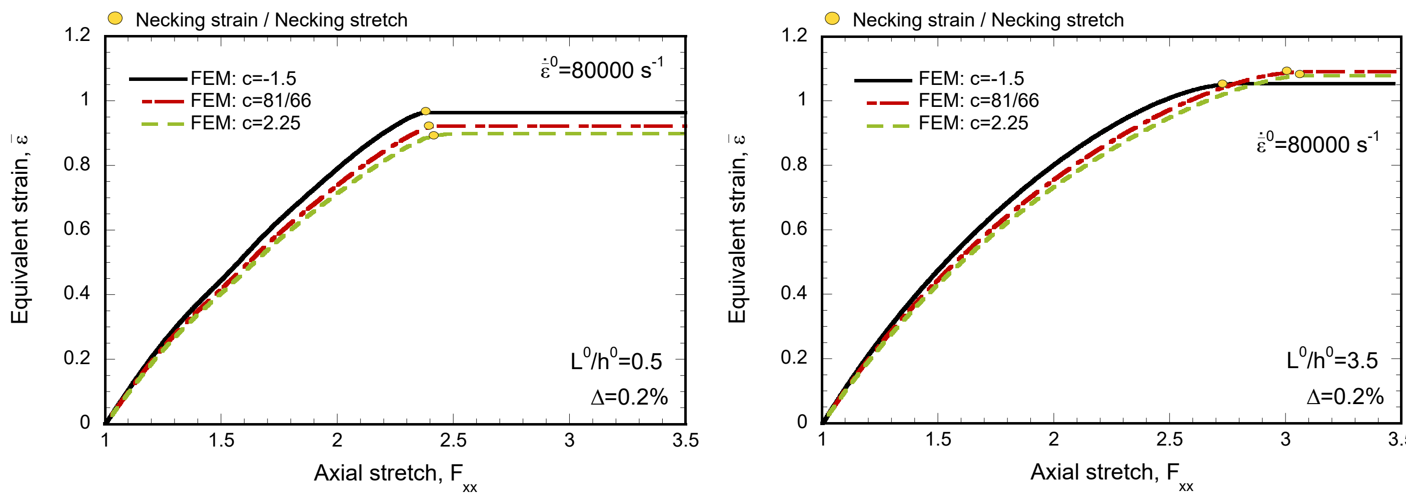

(a) (b)

Figure 14: Finite element results obtained with Drucker yield criterion [11] for Material 2 ($c = -1.5$ and $\sigma_T/\tau_Y = 1.674$), Material 3 (Hershey-Hosford for a BCC material, $c = 81/66$ and $\sigma_T/\tau_Y = 1.790$) and Material 4 ($c = 2.25$ and $\sigma_T/\tau_Y = 1.852$), respectively. The initial equivalent strain rate is $\dot{\bar{\varepsilon}}^0 = 80000$ s^{-1}. The amplitude of the imperfection is $\Delta = 0.2\%$. Equivalent strain $\bar{\varepsilon}$ versus axial stretch F_{xx}. (a) $L^0/h^0 = 0.5$ and (b) $L^0/h^0 = 3.5$.

an increase of one order of magnitude in the elongation of the cell when necking occurs, and boosts the necking strain from 0.12 to 1.05 (775% increase). The comparison with Fig. 15(a) makes apparent that the influence of inertia on the necking strain and the necking stretch is more important as the wavelength increases.

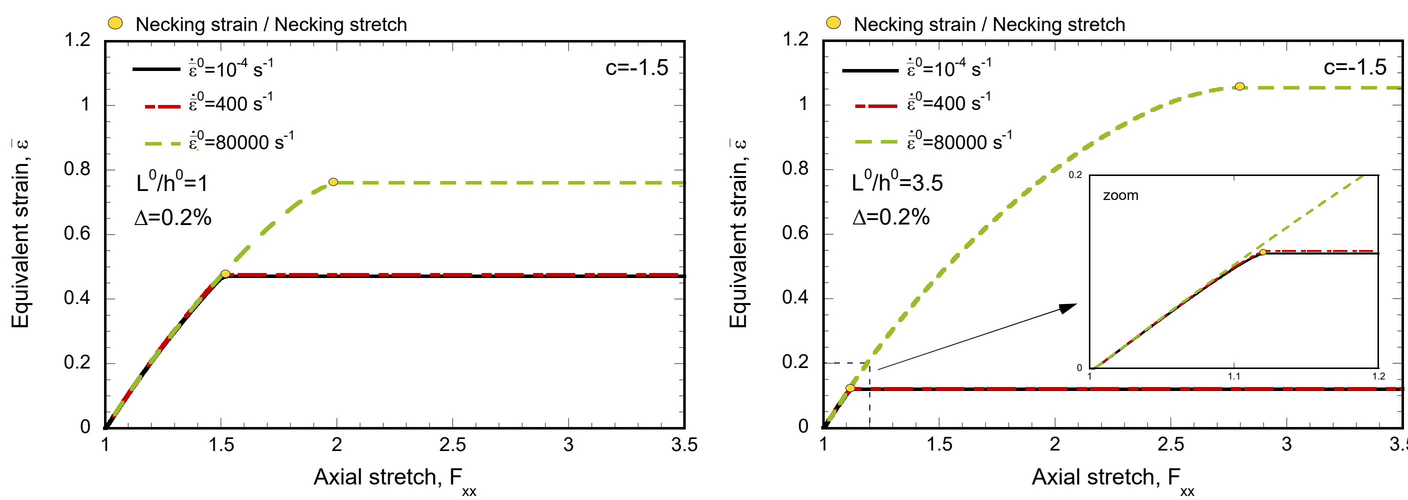

(a) (b)

Figure 15: Finite element results obtained with Drucker yield criterion [11] for Material 2 ($c = -1.5$). Three different initial equivalent strain rates $\dot{\bar{\varepsilon}}^0$ are considered: 10^{-4} s^{-1}, 400 s^{-1} and 80000 s^{-1}. The amplitude of the imperfection is $\Delta = 0.2\%$. Equivalent strain $\bar{\varepsilon}$ versus axial stretch F_{xx}. (a) $L^0/h^0 = 1$ and (b) $L^0/h^0 = 3.5$.

Fig. 16 presents a comparison between finite element results and stability analysis predictions for the evolution of the critical necking wavelength $\left(L^0/h^0\right)_c$ and the critical necking strain $\bar{\varepsilon}_c^{neck}$ with the imposed initial equivalent strain rate $\dot{\bar{\varepsilon}}^0$. Results are shown for Materials 2, 3 and 4 (i.e. $c = -1.5$, $c = 81/66$ and $c = 2.25$). Note that the critical necking wavelength $\left(L^0/h^0\right)_c$ corresponds to the critical cell size obtained from the unit-cell calculations and to the critical cumulative perturbation wavelength derived from the stability analysis for $I_c = 3.75$ (see Figs. 6 and 7). On the other hand, the critical necking strain $\bar{\varepsilon}_c^{neck}$ is the necking strain corresponding to the critical cell size in the finite element calculations and the equivalent strain corresponding to the critical cumulative perturbation wavelength in the stability analysis (see Fig. 6).

The $\left(L^0/h^0\right)_c - \dot{\bar{\varepsilon}}^0$ curves shown in Fig. 16(a) display a concave-upwards shape, so that the critical necking wavelength decreases nonlinearly with the strain rate [15, 42, 55], being the slope of the $\left(L^0/h^0\right)_c - \dot{\bar{\varepsilon}}^0$ curves smaller as $\dot{\bar{\varepsilon}}^0$ increases [40]. The $\bar{\varepsilon}_c^{neck} - \dot{\bar{\varepsilon}}^0$ curves shown in Fig. 16(b) display a concave-downwards shape, so that the critical necking strain $\bar{\varepsilon}_c^{neck}$ increases nonlinearly with the initial equivalent strain rate $\dot{\bar{\varepsilon}}^0$ due to the effect of inertia [47]. The finite element simulations and the stability analysis predictions are in reasonable agreement for the three materials considered and for the whole range of strain rates investigated. Notice that the the effect of the third invariant of the stress deviator on the critical necking wavelength and the critical necking strain is very small.

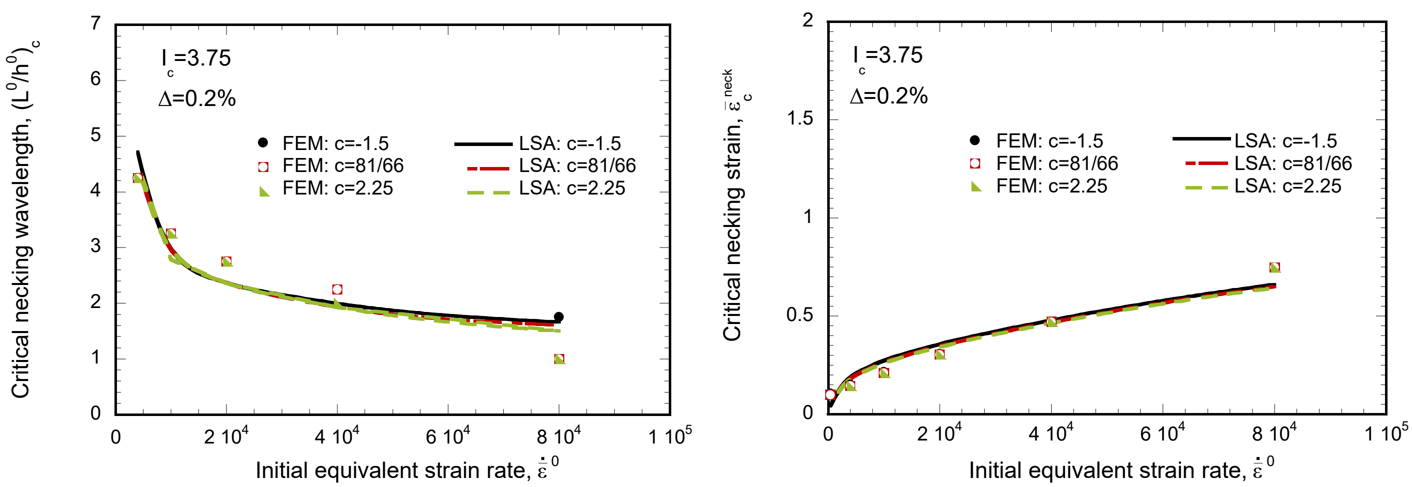

(a) (b)

Figure 16: Comparison between finite element results and stability analysis predictions. (a) Evolution of the critical necking wavelength $\left(L^0/h^0\right)_c$ with the imposed initial equivalent strain rate $\dot{\bar{\varepsilon}}^0$. (b) Evolution of the critical necking strain $\bar{\varepsilon}_c^{neck}$ with the imposed initial equivalent strain rate $\dot{\bar{\varepsilon}}^0$. Calculations are performed with Drucker yield criterion [11] for Material 2 ($c = -1.5$ and $\sigma_T/\tau_Y = 1.674$), Material 3 (Hershey-Hosford for a BCC material, $c = 81/66$ and $\sigma_T/\tau_Y = 1.790$) and Material 4 ($c = 2.25$ and $\sigma_T/\tau_Y = 1.852$), respectively. In the finite element simulations the amplitude of the imperfection is $\Delta = 0.2\%$. In the linear stability analysis the critical cumulative instability index is $I_c = 3.75$.

7. Concluding remarks

In this paper we have investigated, using finite element simulations and linear stability analysis, the formation of necking instabilities in thin plates subjected to plane strain tension and modeled with Drucker yield criterion [11]. The finite element calculations have been performed with ABAQUS [1], using the unit-cell model developed by Xue et al. [50], who considered the plate as an array of unit-cells with sinusoidal geometric imperfections to trigger necking localization. The linear stability analysis extends the model developed by N'souglo et al. [35] to consider materials with yielding governed by Drucker criterion [11]. For this class of materials, yielding depends on both the second and the third invariant of the stress deviator, and a parameter c which accounts for the ratio between the yield stresses in uniaxial tension and in pure shear σ_T/τ_Y. A key point of this work is that we have derived an explicit expression for the strain rate potential under plane strain tension which shows that the rate of accumulation of plastic deformation decreases with the value of c, so that materials with $c < 0$ $\left(\sigma_T/\tau_Y < \sqrt{3}\right)$ display greater rate of accumulation of plastic deformation than a von Mises material ($c = 0$) and materials with $c > 0$ $\left(\sigma_T/\tau_Y > \sqrt{3}\right)$. Using the calibration developed by N'souglo et al. [35], who identified that a perturbation mode turns into a necking mode when the cumulative instability index reaches a specific critical value, we have compared the stability analysis predictions with the finite element results for a wide range of necking wavelengths $L^0/h^0 \leqslant 6$ and imposed initial equivalent strain rates $\dot{\bar{\varepsilon}}^0$ varying from 10^{-4} s^{-1} to $8 \cdot 10^4$ s^{-1}. In addition, we have compared perturbation analysis results obtained with both cumulative and instantaneous instability index, showing that, while for low strain rates the predictions obtained using both criteria are very similar, at high strain rates the cumulative index provides results which find better agreement with the finite element calculations. Moreover, the analysis developed in this paper has revealed that, for any given value of $\dot{\bar{\varepsilon}}^0$, the initial strain rate in the loading direction of the specimen increases as σ_T/τ_Y increases (i.e. as c increases and the rate of accumulation of plastic deformation decreases). This was put into evidence by considering four model materials that are characterized by the same elastic behavior, initial yield stress and hardening in simple tension, and only differ in the ratio between the yield stresses in uniaxial tension and in pure shear. Finite element results and stability analysis predictions obtained with the cumulative instability index show the same overall trends for the necking strain $\bar{\varepsilon}^{neck}$ and the necking stretch F_{xx}^{neck} for the materials investigated, and there is also reasonable quantitative agreement for most of the strain rates and necking wavelengths considered. In addition, we have shown that the linear stability analysis predicts the increase of the critical necking strain and the decrease of the critical necking wavelength with the initial equivalent strain rate. This is a key outcome of our investigation which shows that the linear stability analysis, despite several simplifying assumptions (two-dimensional character, linear nature, frozen perturbation coefficients, Bridgman correction, etc.), shows remarkable capacity to predict necking localization in Drucker materials subjected to plane strain stretching. In addition, we have shown that for initial equivalent strain rates below 10^4 s^{-1}, the necking stretch is virtually independent of the value of c for all the necking wavelengths investigated, and the necking strain is greater for materials with $c < 0$ than for von Mises material ($c = 0$) and materials with ($c > 0$). This was explained based on the dependence of the plastic dissipation on c (see equation (21)). At higher equivalent strain rates, the effect of the value of c on the necking strain and the necking stretch becomes wavelength dependent. Specifically, while for short wavelengths the effect of c is the same as in the case of lower strain rates, for long wavelengths the smallest necking strain corresponds to the material which displays the highest rate of accumulation of plastic deformation. An important result of this paper is to demonstrate that the reason for this behavior is the wavelength dependent influence of inertia on necking localization. For high initial equivalent strain rates and long necking wavelengths, the necking stretch is primarily determined by the strain rate in the axial direction of the specimen, which increases as the rate of accumulation of plastic deformation in the material decreases, delaying localization and boosting the necking strain.

Funding

JAR-M and KEN acknowledge the financial support provided by the European Research Council (ERC) under the European Union's Horizon 2020 research and innovation programme. Project PURPOSE, grant agreement 758056.

OC acknowledges partial support provided by AFOSR grant FA9550-18-1-0517 and the support during her sabbatical at the UC3M through the Programa Cátedras de Excelencia UC3M-Santander.

Appendix A. Stability analysis results and finite element calculations with prescribed stretch rate

In this section, we show finite element results and stability analysis predictions obtained imposing the initial axial strain rate $\dot{\varepsilon}^0_{xx}$ as the loading condition, instead of the initial equivalent strain rate $\dot{\bar{\varepsilon}}^0$, as in all other calculations performed in this work (see Section 3.1). The results correspond to Material 2 ($c = -1.5$), Material 3 ($c = 81/66$) and Material 4 ($c = 2.25$). The stability analysis predictions are obtained with the critical cumulative instability index $I_c = 3.75$. We also include finite element results for Material 2 imposing the initial equivalent strain rate.

Figs. A.17(a) and A.17(b) show the evolution of the necking strain $\bar{\varepsilon}^{neck}$ and the necking stretch F_{xx}^{neck} with L^0/h^0 for $\dot{\varepsilon}_{xx}^0 = 4000$ s^{-1}. The results obtained for the three materials are very similar to those reported Figs. 10(a) and 10(b) for an imposed initial equivalent strain rate of $\dot{\bar{\varepsilon}}^0 = 4000$ s^{-1}. Moreover, Figs. A.18(a) and A.18(b) display the $\bar{\varepsilon}^{neck} - L^0/h^0$ and $F_{xx}^{neck} - L^0/h^0$ curves for $\dot{\varepsilon}_{xx}^0 = 80000$ s^{-1}. The results are also quantitatively similar to those reported in Figs. 13(a) and 13(b) for $\dot{\bar{\varepsilon}}^0 = 80000$ s^{-1}, suggesting that imposing either the initial equivalent strain rate or the initial stretch rate in the calculations yields similar results. However, there are qualitative differences on the effect of the parameter c on the necking strain and the necking stretch. Specifically, both finite element calculations and stability analysis predictions presented in Fig. A.18(a) show that for $\dot{\varepsilon}_{xx}^0 = 80000$ s^{-1} the necking strain is greater as the parameter c decreases (i.e. as the rate of accumulation of plastic deformation increases), while this is not the case when the initial equivalent strain rate is imposed, since the smaller necking strain for long wavelengths corresponds to $c = -1.5$ (see Fig. 13(a)). In addition, Fig. A.18(b) shows that, while the relative order of the $F_{xx}^{neck} - L^0/h^0$ curves for the three materials is the same obtained for $\dot{\bar{\varepsilon}}^0 = 80000$ s^{-1}, the difference in the necking stretch for the whole range of wavelengths is less (see Fig. 13(b)).

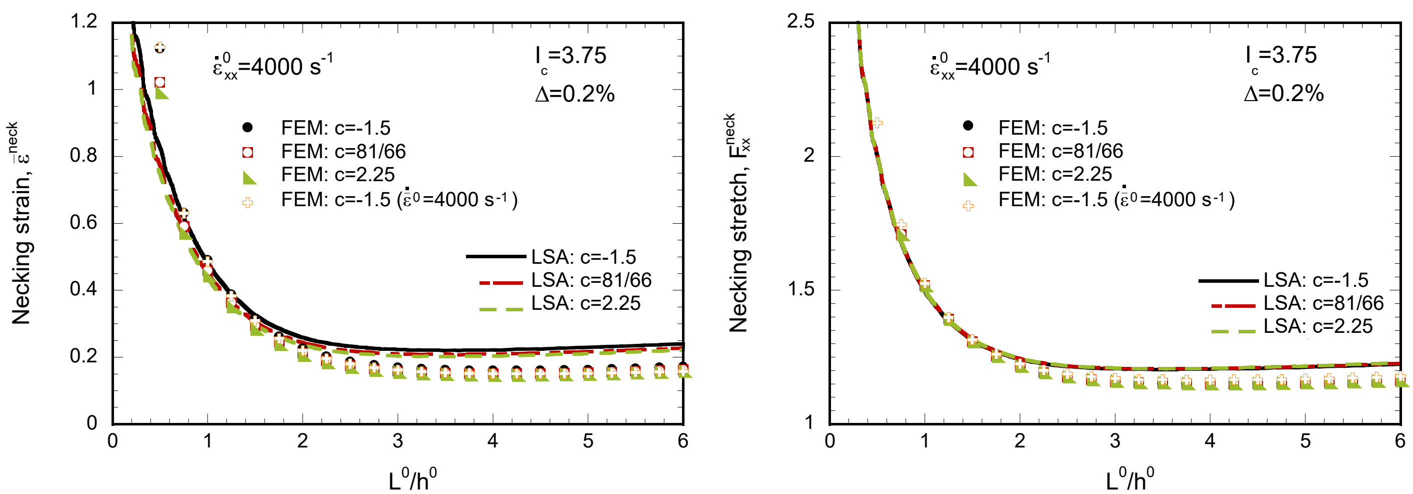

Figure A.17: Comparison between finite element results (FEM) and linear stability analysis predictions (LSA) obtained with Drucker yield criterion [11] for Material 2 ($c = -1.5$ and $\sigma_T/\tau_Y = 1.674$), Material 3 (Hershey-Hosford for a BCC material, $c = 81/66$ and $\sigma_T/\tau_Y = 1.790$) and Material 4 ($c = 2.25$ and $\sigma_T/\tau_Y = 1.852$), respectively. The initial stretch rate along the axial direction is $\dot{\varepsilon}_{xx}^0 = 4000$ s^{-1}. (a) Necking strain $\bar{\varepsilon}^{neck}$ versus L^0/h^0. (b) Necking stretch F_{xx}^{neck} versus L^0/h^0. In the finite element simulations the amplitude of the imperfection is $\Delta = 0.2\%$. In the linear stability analysis the critical cumulative instability index is $I_c = 3.75$. We also include finite element results for Material 2 ($c = -1.5$) imposing the initial equivalent strain rate $\dot{\bar{\varepsilon}}^0 = 4000$ s^{-1}.

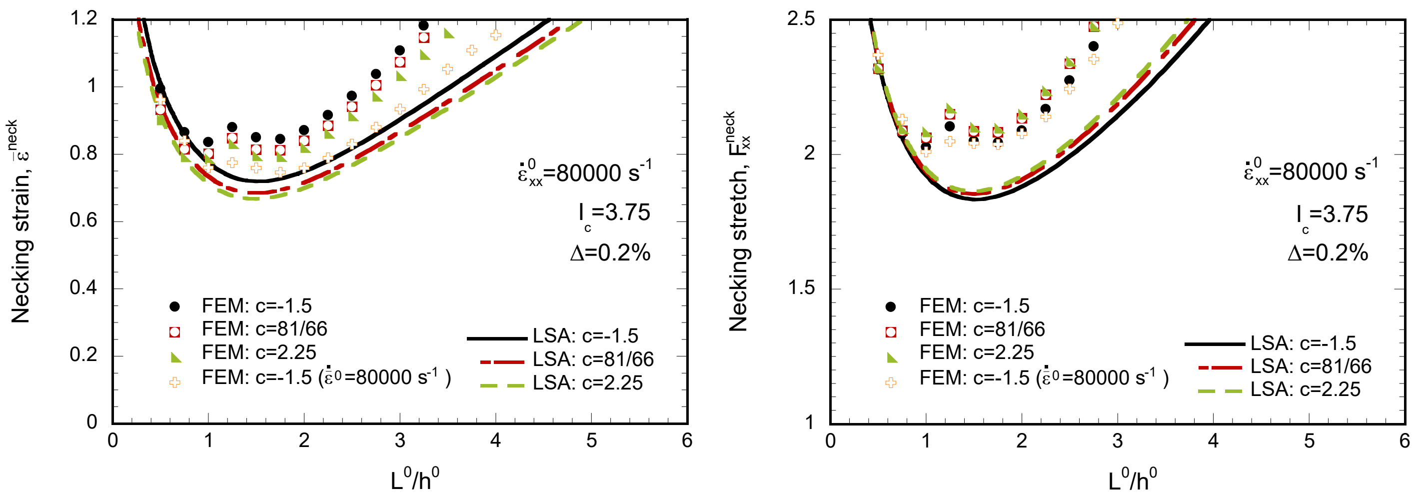

(a) (b)

Figure A.18: Comparison between finite element results (FEM) and linear stability analysis predictions (LSA) obtained with Drucker yield criterion [11] for Material 2 ($c = -1.5$ and $\sigma_T/\tau_Y = 1.674$), Material 3 (Hershey-Hosford for a BCC material, $c = 81/66$ and $\sigma_T/\tau_Y = 1.790$) and Material 4 ($c = 2.25$ and $\sigma_T/\tau_Y = 1.852$), respectively. The initial stretch rate along the axial direction is $\dot{\varepsilon}^0_{xx} = 80000$ s^{-1}. (a) Necking strain $\bar{\varepsilon}^{neck}$ versus L^0/h^0. (b) Necking stretch F^{neck}_{xx} versus L^0/h^0. In the finite element simulations the amplitude of the imperfection is $\Delta = 0.2\%$. In the linear stability analysis the critical cumulative instability index is $I_c = 3.75$. We also include finite element results for Material 2 ($c = -1.5$) imposing the initial equivalent strain rate $\dot{\bar{\varepsilon}}^0 = 80000$ s^{-1}.

Appendix B. Additional comparison between critical instantaneous instability index and critical cumulative instability index

In this section, we present additional comparisons between the predictions obtained with the critical instantaneous instability index $\hat{\eta}_c^+ = 19$ and the critical cumulative instability index $I_c = 3.75$ for Material 1 (von Mises material, $c = 0$). Namely, Fig. B.19 shows the evolution of the necking strain $\bar{\varepsilon}^{neck}$ with L^0/h^0 for five different initial equivalent strain rates $\dot{\bar{\varepsilon}}^0 = 400$ s^{-1}, 4000 s^{-1}, 10000 s^{-1}, 20000 s^{-1} and 80000 s^{-1}. The stability analysis results are compared with finite element calculations.

For the lower initial equivalent strain rates, 400 s^{-1}, 4000 s^{-1} and 10000 s^{-1}, the predictions of the stability analysis with both criteria are similar (especially for 400 s^{-1}), and find qualitative and quantitative agreement with the finite element calculations, being the predictions obtained with $\hat{\eta}_c^+ = 19$ closer to the numerical simulations. On the other hand, for greater initial equivalent strain rates, there are important differences between the results obtained with $\hat{\eta}_c^+ = 19$ and $I_c = 3.75$ so that, contrary to what occurs at lower strain rates, for long wavelengths the instantaneous instability index predicts values of the necking strain greater than the cumulative instability index (see also Fig. 6). The different results obtained with both criteria are particularly noticeable for 80000 s^{-1}, for this strain rate the predictions with $I_c = 3.75$ being much closer to the finite element calculations than the results obtained with $\hat{\eta}_c^+ = 19$, showing that the analytical predictions based on the instantaneous instability index overestimate the role of inertia on the necking strain.

Appendix C. Stability analysis results with strain rate dependent critical cumulative instability index

In this section, we compare finite element results with stability analysis predictions obtained using strain rate dependent critical cumulative index. The calculations are performed with Material 1 (von Mises material, $c = 0$ and $\sigma_T/\tau_Y = \sqrt{3}$), and the results correspond to four different initial equivalent strain rates: 400 s^{-1}, 10000 s^{-1}, 20000 s^{-1} and 80000 s^{-1}. The critical cumulative instability index is taken to be a second order polynomial $I_c = F + G\,\dot{\bar{\varepsilon}}^0 + H\,(\dot{\bar{\varepsilon}}^0)^2$, whose coefficients $F = 0.96454$, $G = 8.883 \cdot 10^{-5}$ and $H = -4.7983 \cdot 10^{-10}$ have been determined obtaining the value of I_c for three initial equivalent strain rates, 400 s^{-1}, 40000 s^{-1} and 80000 s^{-1}, following the methodology discussed in Section 6.1. Similar procedure has been recently used by Jacques and Rodríguez-Martínez [25] to determine the evolution of the critical cumulative index with the strain rate, to predict multiple necking formation in viscoplastic metallic bars subjected to dynamic stretching.

Fig. C.20 shows that the stability analysis predictions obtained with strain rate dependent critical cumulative index are in quantitative agreement with the unit-cell calculations, within the whole range of wavelengths investigated, and for all the strain rates considered (including strain rates other than those used to calibrate I_c). It becomes apparent that accounting for the strain rate dependence of I_c improves the predictions of the stability analysis, yet at the expense of needing additional calibration data. A throughout discussion of the pros and cons of considering the functional dependence of I_c on the strain rate is left for a future work.

Conflict of interest

The authors declare that they have no conflict of interest.

References

[1] ABAQUS, 2016. Abaqus v6.16 User's Manual. version 6.16 ed., ABAQUS Inc., Richmond, USA.

[2] Altynova, M., Hu, X., Daehn, G.S., 1996. Increased ductility in high velocity electromagnetic ring expansion. Metallurgical Transactions A 27, 1837–1844.

[3] Barlat, F., 1987. Crystallographic texture, anisotropic yield surfaces and forming limits of sheet metals. Materials Science and Engineering 91, 55 – 72.

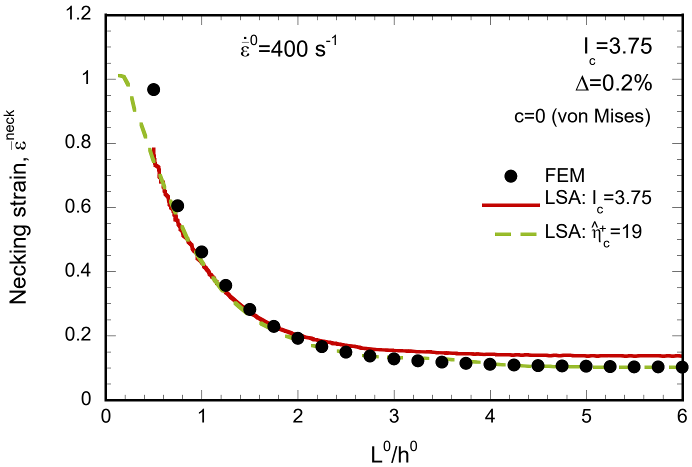

(a)

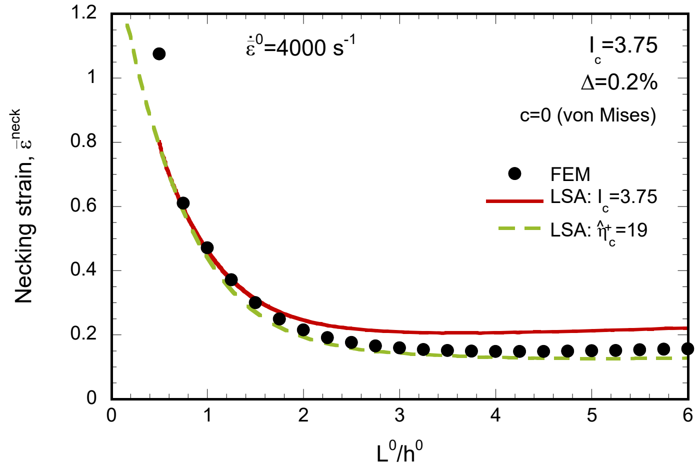

(b)

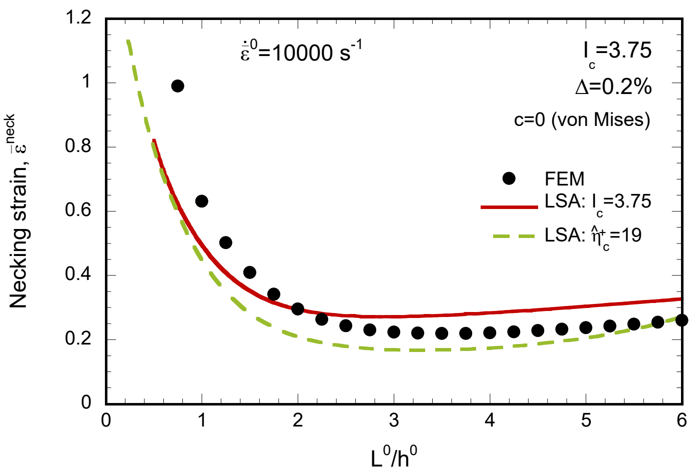

(c)

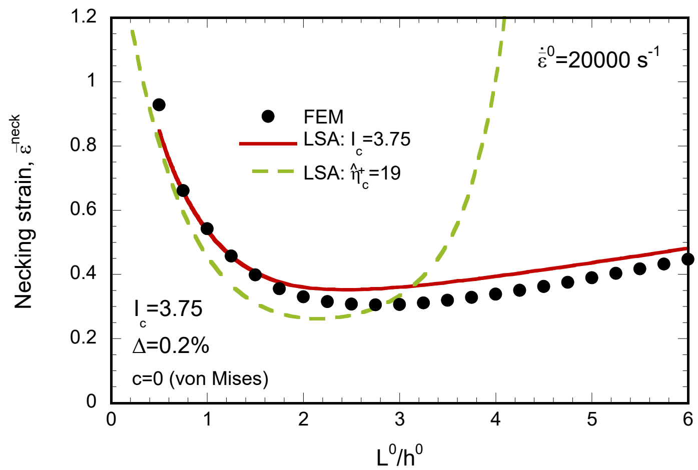

(d)

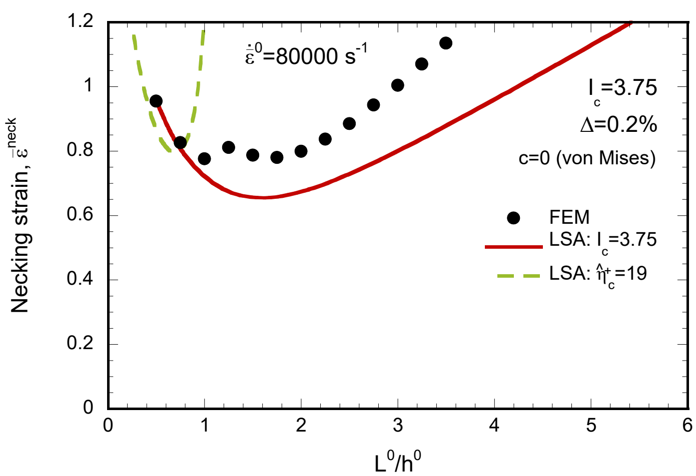

(e)

Figure B.19: Necking strain $\bar{\varepsilon}^{neck}$ versus L^0/h^0. Comparison between finite element results (FEM) and linear stability analysis predictions (LSA) obtained with Material 1 (von Mises material, $c = 0$ and $\sigma_T/\tau_Y = \sqrt{3}$). The initial equivalent strain rate is: (a) $\dot{\bar{\varepsilon}}^0 = 400$ s^{-1}, (b) $\dot{\bar{\varepsilon}}^0 = 4000$ s^{-1}, (c) $\dot{\bar{\varepsilon}}^0 = 10000$ s^{-1}, (d) $\dot{\bar{\varepsilon}}^0 = 20000$ s^{-1} and (e) $\dot{\bar{\varepsilon}}^0 = 80000$ s^{-1}. In the finite element simulations the amplitude of the imperfection is $\Delta = 0.2\%$. Linear stability analysis results are shown for the critical cumulative instability index $I_c = 3.75$, and the critical instantaneous instability index $\hat{\eta}_c^+ = 19$.

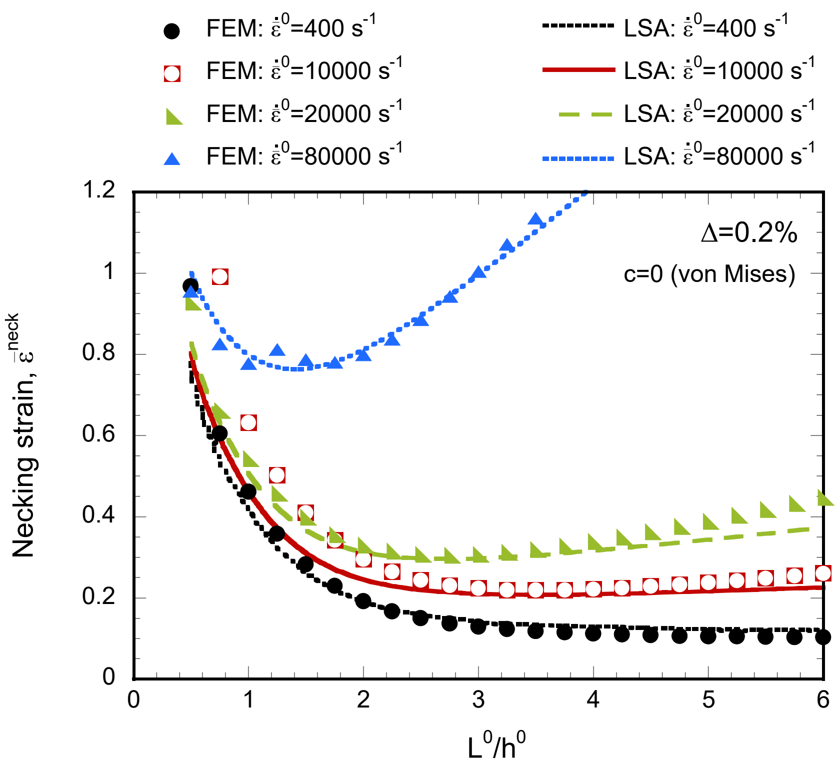

Figure C.20: Necking strain $\bar{\varepsilon}^{neck}$ versus L^0/h^0. Comparison between finite element results (FEM) and linear stability analysis predictions (LSA) obtained for Material 1 (von Mises material, $c = 0$ and $\sigma_T/\tau_Y = \sqrt{3}$). The results correspond to four different initial equivalent strain rates $\dot{\bar{\varepsilon}}^0 = 400\ \mathrm{s}^{-1}$, $10000\ \mathrm{s}^{-1}$, $20000\ \mathrm{s}^{-1}$ and $80000\ \mathrm{s}^{-1}$. In the finite element simulations the amplitude of the imperfection is $\Delta = 0.2\%$. In the linear stability analysis the critical cumulative instability index is taken strain rate dependent $I_c = 0.96454 + 8.883 \cdot 10^{-5}\, \dot{\bar{\varepsilon}}^0 - 4.7983 \cdot 10^{-10} \cdot \left(\dot{\bar{\varepsilon}}^0\right)^2$.

[4] Bridgman, P.W., 1952. Studies in large plastic flow and fracture, with special emphasis on the effects of hydrostatic pressure, vol.1. McGraw-Hill Book Company, Inc., New York.

[5] Butuc, M.C., Gracio, J.J., Barata da Rocha, A., 2003. A theoretical study on forming limit diagrams prediction. Journal of Materials Processing Technology 142, 714 – 724.

[6] Cazacu, O., 2019. New mathematical results and explicit expressions in terms of the stress components of Barlat et al. (1991) orthotropic yield criterion. International Journal of Solids and Structures 176-177, 86 – 95.

[7] Cazacu, O., Plunkett, B., Barlat, F., 2006. Orthotropic yield criterion for hexagonal closed packed metals. International Journal of Plasticity 22, 1171–1194.

[8] Cazacu, O., Revil-Baudard, B., Chandola, N., 2019. Springer International Publishing.

[9] Chou, P.C., Carleone, J., 1977. The stability of shaped-charge jets. Journal of Applied Physics 48, 4187–4195.

[10] Considère, A., 1885. Mémoire sur l'emploi du fer et de l'acier dans les constructions. Ann. Ponts et Chaussées 9, 574–775.

[11] Drucker, D.C., 1949. Relation of experiments to mathematical theories of plasticity. Journal of Applied Mechanics 16, 349–357.

[12] Dudzinski, D., Molinari, A., 1991. Perturbation analysis of thermoviscoplastic instabilities in biaxial loading. International Journal of Solids and Structures 27, 601–628.

[13] El Maï, S., Mercier, S., Petit, J., Molinari, A., 2014. An extension of the linear stability analysis for the prediction of multiple necking during dynamic extension of round bar. International Journal of Solids and Structures 51, 3491–3507.

[14] Fressengeas, C., Molinari, A., 1985. Inertia and thermal effects on the localization of plastic flow. Acta Metallurgica 33, 387–396.

[15] Fressengeas, C., Molinari, A., 1994. Fragmentation of rapidly stretching sheets. European Journal of Mechanics A/Solids 13, 251–268.

[16] Grady, D.E., Benson, D.A., 1983. Fragmentation of metal rings by electromagnetic loading. Experimental Mechanics 12, 393–400.

[17] Guduru, P.R., Freund, L.B., 2002. The dynamics of multiple neck formation and fragmentation in high rate extension of ductile materials. International Journal of Solids and Structures 39, 5615–5632.

[18] Gurson, A., 1977. Continuum theory of ductile rupture by void nucleation and growth. Part I: Yield criteria and flow rules for porous ductile media. ASME Journal of Engineering Materials and Technology 99, 2–15.

[19] Hershey, A.V., 1954. The plasticity of an isotropic aggregate of anisotropic face centered cubic crystals. Journal of Applied Mechanics 76, 241–249.

[20] Hill, R., 1948. A theory of the yielding and plastic flow of anisotropic metals, in: Proceedings of the Royal Society of London A: Mathematical, Physical and Engineering Sciences, The Royal Society. pp. 281–297.

[21] Hill, R., Hutchinson, J.W., 1975. Bifurcation phenomena in the plane tension test. Journal of the Mechanics and Physics of Solids 23, 239–264.

[22] Hosford, W.F., 1979. On yield loci of anisotropic cubic metals, in: Proceedings of the seventh North American metalworking research conference, pp. 191–196.

[23] Hutchinson, J.W., Neale, K., Needleman, A., 1978. Mechanics of sheet metal forming. Plenum Press, New York/London. pp. 269–285.

[24] Jacques, N., 2020. An analytical model for necking strains in stretched plates under dynamic biaxial loading. International Journal of Solids and Structures 200-201, 198 – 212.

[25] Jacques, N., Rodríguez-Martínez, J.A., 2020. Influence on strain-rate history effects on the development of necking instabilities under dynamic loading conditions . Submitted for Publication .

[26] Jouve, D., 2013. Analytic study of plastic necking instabilities during plane tension tests. European Journal of Mechanics - A/Solids 39, 180 – 196.

[27] Jouve, D., 2015. Analytic study of the onset of plastic necking instabilities during biaxial tension tests on metallic plates. European Journal of Mechanics - A/Solids 50, 59 – 69.

[28] Karpp, R.R., Simon, J., 1976. An estimate of the strength of a copper shaped charge jet and the effect of strength on the breakup of a stretching jet. Technical Report. U.S. Army Ballistic Research Laboratories (BRL).

[29] Marciniak, Z., Kuczyński, K., 1967. Limit strains in the processes of stretch-forming sheet metal. International Journal of Mechanical Sciences 9, 609 – 620.

[30] Mercier, S., Granier, N., Molinari, A., Llorca, F., Buy, F., 2010. Multiple necking during the dynamic expansion of hemispherical metallic shells, from experiments to modelling. Journal of the Mechanics and Physics of Solids 58, 955–982.

[31] Mercier, S., Molinari, A., 2004. Analysis of multiple necking in rings under rapid radial expansion. International Journal of Impact Engineering 30, 403–419.

[32] Mises, R.V., 1928. Mechanik der plastischen formänderung von kristallen. ZAMM - Journal of Applied Mathematics and Mechanics / Zeitschrift für Angewandte Mathematik und Mechanik 8, 161–185.

[33] Niordson, F.L., 1965. A unit for testing materials at high strain rates. Experimental Mechanics 5, 29–32.

[34] N'souglo, K.E., Jacques, N., Rodríguez-Martínez, J.A., 2021. A three-pronged approach to predict the effect of plastic orthotropy on the formability of thin sheets subjected to dynamic biaxial stretching. Journal of the Mechanics and Physics of Solids 146, 104189.

[35] N'souglo, K.E., Rodríguez-Martínez, J.A., Cazacu, O., 2020. The effect of tension-compression asymmetry on the formation of dynamic necking instabilities under plane strain stretching. International Journal of Plasticity 128, 102656.

[36] N'souglo, K.E., Srivastava, A., Osovski, S., Rodríguez-Martínez, J.A., 2018. Random distributions of initial porosity trigger regular necking patterns at high strain rates. Proceedings of the Royal Society A: Mathematical, Physical and Engineering Sciences 474, 20170575.

[37] Parmar, A., Mellor, P.B., 1978. Predictions of limit strains in sheet metal using a more general yield criterion. International Journal of Mechanical Sciences 20, 385 – 391.

[38] Petit, J., Jeanclaude, V., Fressengeas, C., 2005. Breakup of copper shaped-charge jets: Experiment, numerical simulations, and analytical modeling. Journal of Applied Physics 98, 123521.

[39] Rodríguez-Martínez, J.A., Molinari, A., Zaera, R., Vadillo, G., Fernández-Sáez, J., 2017. The critical neck spacing in ductile plates subjected to dynamic biaxial loading: On the interplay between loading path and inertia effects. International Journal of Solids and Structures 108, 74–84.

[40] Rodríguez-Martínez, J.A., Vadillo, G., Fernández-Sáez, J., Molinari, A., 2013. Identification of the critical wavelength responsible for the fragmentation of ductile rings expanding at very high strain rates. Journal of the Mechanics and Physics of Solids 61, 1357–1376.

[41] Rodríguez-Martínez, J.A., Vadillo, G., Zaera, R., Fernández-Sáez, J., Rittel, D., 2015. An analysis of microstructural and thermal softening effects in dynamic necking. Mechanics of Materials 80, 298 – 310. IUTAM Symposium on materials and interfaces under high strain rate and large deformation.

[42] Shenoy, V.B., Freund, L.B., 1999. Necking bifurcations during high strain rate extension. Journal of the Mechanics and Physics of Solids 47, 2209–2233.

[43] Sowerby, R., Duncan, J.L., 1971. Failure in sheet metal in biaxial tension. International Journal of Mechanical Sciences 13, 217 – 229.

[44] Stören, S., Rice, J., 1975. Localized necking in thin sheets. Journal of the Mechanics and Physics of Solids 23, 421–441.

[45] Tvergaard, V., 1982. On localization in ductile materials containing spherical voids. International Journal of Fracture 18, 237–252.

[46] Tvergaard, V., Needleman, A., 1984. Analysis of the cup-cone fracture in a round tensile bar. Acta Metallurgica 32, 157–169.

[47] Vaz-Romero, A., Rodríguez-Martínez, J.A., Mercier, S., Molinari, A., 2017. Multiple necking pattern in nonlinear elastic bars subjected to dynamic stretching: The role of defects and inertia. International Journal of Solids and Structures 125, 232–243.

[48] Walsh, J.M., 1984. Plastic instability and particulation in stretching metals jets. Journal of Applied Physics 56, 1997–2006.

[49] Xavier, M., Czarnota, C., Jouve, D., Mercier, S., Dequiedt, J.L., Molinari, A., 2020. Extension of linear stability analysis for the dynamic stretching of plates: Spatio-temporal evolution of the perturbation. European Journal of Mechanics - A/Solids 79, 103860.

[50] Xue, Z., Vaziri, A., Hutchinson, J.W., 2008. Material aspects of dynamic neck retardation. Journal of the Mechanics and Physics of Solids 56, 93–113.

[51] Zaera, R., Rodríguez-Martínez, J.A., Vadillo, G., Fernández-Sáez, J., 2014. Dynamic necking in materials with strain induced martensitic transformation. Journal of the Mechanics and Physics of Solids 64, 316–337.

[52] Zaera, R., Rodríguez-Martínez, J.A., Vadillo, G., Fernández-Sáez, J., Molinari, A., 2015. Collective behaviour and spacing of necks in ductile plates subjected to dynamic biaxial loading. Journal of the Mechanics and Physics of Solids. 85, 245–269.

[53] Zhang, H., Ravi-Chandar, K., 2010. On the dynamics of localization and fragmentation-IV. Expansion of Al 6061-O tubes. International Journal of Fracture 163, 41–65.

[54] Zheng, X., N'souglo, K.E., Rodríguez-Martínez, J.A., Srivastava, A., 2020. Dynamics of necking and fracture in ductile porous materials. Journal of Applied Mechanics - Transactions of the ASME 87, 41005.

[55] Zhou, F., Molinari, J.F., Ramesh, K.T., 2006. An elasto-visco-plastic analysis of ductile expanding ring. International Journal of Impact Engineering 33, 880–891.